

A Tool for Estimating Ground-Based InSAR Acquisition Characteristics Prior to Monitoring Installation and Survey, and Its Differences from Satellite InSAR

Charlotte Wolff¹, Marc-Henri Derron¹, Carlo Rivolta², Michel Jaboyedoff¹

5 ¹ISTE, University of Lausanne, Lausanne, 1015, Switzerland

²Ellegi srl, Milano, 20123, Italy

Correspondence to: Charlotte Wolff (charlotte.wolff@unil.ch)

Abstract. Synthetic Aperture Radar (SAR) acquisition can be performed from satellites or from the ground by means of a so-called GB-InSAR (Ground-Based Interferometry SAR), but the signal emission and the output image geometry slightly differ
10 between the two acquisition modes. Those differences are rarely mentioned in the literature. This paper proposes to compare satellite and GB-InSAR in terms of (1) acquisition characteristics and parameters to consider; (2) SAR image resolution; (3) geometric distortions that are foreshortening, layover and shadowing.

If in the case of satellites SAR, the range and azimuth resolutions are known and constant along the orbit path, in the case of GB-InSAR their values are terrain-dependent. It is worth estimating the results of a GB-InSAR acquisition one can expect in
15 terms of range and azimuth resolution, Line of Sight (LoS) distance and geometric distortions to select the best installation location when several are possible. We developed a novel tool which estimates those parameters from a Digital Elevation Model (DEM), knowing the GB-InSAR and the Slope of Interest (SoI) coordinates. This tool, written in MATLAB, was tested on a simple synthetic point cloud representing a cliff with a progressive slope angle to highlight the influence of the SoI geometry on the acquisition characteristics and on two real cases; cliffs located in Switzerland, one in the Ticino canton and
20 on in the Vaud canton.

1 Introduction

The use of Synthetic Aperture Radar Interferometry (InSAR) as a remote sensing technique capable of detecting and monitoring small ground displacements started in the 80s (Gabriel et al. 1989). It was initially used specifically with space borne platforms such as satellites ERS-1 (1991) or RADAR-SAT (1995, Zebker et Villasenor 1992; Massonnet et al. 1993;
25 Usai et Hanssen 1997). In the field of geosciences, it has been primarily dedicated to studying small movements phenomena (less than cm) across large areas (km) with a resolution ranging from decametric to metric scales, such as subsidence (Cabral-Cano et al., 2008; Strozzi et al., 2018), volcanic activities (Wicks et al. 1998; Garthwaite et al. 2019) or landslides (Tarchi 2003; Hilley et al. 2004; Colesanti et Wasowski 2006). Since then, the technique expanded and by the late 90s first radar devices monitoring displacements from a Ground Base (GB) were deployed (Tarchi et al., 1997; Cazzanil et al., 2000;
30 Pieraccini and Miccinesi, 2019). Some use a Real Aperture Radar (RAR) antenna (Werner et al., 2008) while others employ a Synthetic Aperture Radar (SAR, Rudolf et al., 1999; Leva et al., 2003; Antonello et al., 2003).

Satellite- and GB-InSAR are complementary, both detecting displacements only along their respective Line-of-Sight (LoS) (Casagli et al. 2003; Catani et al. 2014; Carlà et al. 2019). InSAR satellites detect sub-vertical movements while GB-InSAR devices gather information on sub-horizontal movements (Wolff et al., 2023).

35 Radar images acquisition and processing are sensitive to terrain geometry which can have significant effects on the appearance of the resulting radar image such as slope compression and highlighting (foreshortening and layover effects, (Jensen, 2006) or surfaces not illuminated by the radar appearing dark and elongated in the image (shadowing effect). Terrain slopes and radar incidence angle influence the image resolution. Satellite imagery-oriented software creates foreshortening and layover masks (Kropatsch and Strobl, 1990; Rees, 2000). Although SAR satellite geometries are well documented (Griffiths 1995; Rees 2000; 40 McCandLOSess et Jackson 2004; Ferretti et al. 2007), the transposition of these geometries to GB-InSAR is seldom mentioned in literature. Nevertheless, before initiating a new GB-InSAR campaign, it is crucial to estimate what results one can expect in terms of distance to the region of interest, range, and azimuthal resolutions as well as potential foreshortening and shadowing effects; in order to select the best position before starting the campaign. This is particularly the case for the installing a GB-InSAR in remote areas and difficult installation sites (Lingua et al. 2008; Cafduff et al. 2015; Talich 2016; Rouyet et al. 2017). 45 After transposing the SAR geometry described for satellites to ground SAR geometry and presenting the main differences between satellite and GB-InSAR, this paper describes a MATLAB tool with a user interface, designed to compute several parameters of the radar image such as its range and azimuthal resolutions, the areas affected by shadowing or strong foreshortening in the case of a Linear SAR system consisting in a radar measuring head moving along a rail. The needed inputs are a Digital Elevation Model (DEM) in an ascii format, the localization of the area of interest and the localization where one 50 intends to install the GB-InSAR. The main objective is to provide a tool for helping surveyors to find the best installation location.

The tool has been tested across three study cases: (1) a synthetic cliff made of slope angles increasing form the bottom to the top, (2 & 3) two real unstable cliffs that have been monitored with a GB-InSAR, Cima del Simano and La Cornalle. For Cima del Simano, the results for three different radar positions were compared to select the best installation position.

55 2 Theory

Table 1 : List of abbreviations used for the radar characteristics presented here after

Name	Abbreviation	Unit	Definition
Line-of-Sight vector	$\vec{\text{LoS}}$	m	Vector between radar and target points
LoS distance	dLoS	m	Radar-target distance
Distance on slope	D_{slope}	m	Distance of illuminated surface along the slope, in range direction
Look or nadir angle	Φ	$^{\circ}$	Angle between the vertical line and the LOS
Incident angle	θ	$^{\circ}$	Angle between LoS and the normal of the targeted surface

Depression angle	γ	$^{\circ}$	Complement angle to Φ
Apparent Orientation	ω	$^{\circ}$	Horizontal angle between LoS and target slope strike
Slope dip	α	$^{\circ}$	Slope dip
Apparent slope dip	α_{app}	$^{\circ}$	Apparent slope dip seen from radar position
Speed of light	c	$m.s^{-1}$	3.10^8
Radar wavelength	λ	cm	Spatial period of the signal
Frequency	f	GHz	$f=c/\lambda$
Frequency Modulated Pulsed Radar	FMPR	-	Type of radar to which satellite InSAR belongs (Mahafza, 2000; Nadav, 2003)
Frequency Modulated Continuous Wave	FMCW	-	Type of radar to which GB-InSAR belongs (Wolff 1998; Nadav 2003)
Pulse length	τ_{FMPR}	μs	- In the case of satellite InSAR, duration of the emission of one radar pulse
Sweep length	τ_{FMCW}	μs	- In the case of GB-InSAR, duration of one sequence of frequency variation
Pulse Repetition Interval	PRI	μs	- In the case of satellite InSAR, time between the emission of two consecutive radar pulses
Pulse Repetition Frequency	PRF	MHz	$PRF = 1/\tau_{FMPR}$
Frequency Bandwidth	BW	MHz	Difference between the upper and lower cut-off frequencies For satellite InSAR: $BW = 1/\tau_{FMPR}$ (Mahafza, 2000) For GB-InSAR: $BW = 1/\tau_{FMCW}$
Antenna Beamwidth	ε	$^{\circ}$	Angle from which the majority of the antenna's power radiates In the case of GB-InSAR, the vertical and horizontal beamwidths are different and denoted ε_v and ε_h
Illuminated area length	W_{illu}	m	Length of the illuminated area in the case of the GB-InSAR, which increases with the range.
Illuminated area height	H_{illu}	m	Height of the illuminated area in the case of the GB-InSAR
Synthetic antenna length	L	m	- In the case of Linear GB-InSAR, rail length used to focus the radar image (which is shorter than the total rail length). L is generally 2 or 3 m. - In the case of satellite InSAR, L can be several km.
Real antenna length	L_{real}		- In the case of satellite InSAR, radar antenna length
Resolution	R	m	Size of the smallest object detectable by the sensor
Ground range resolution	R_r	m	Resolution (ground pixel size) of the radar image along the Line of Sight

Azimuthal resolution	R_{az}	m	Resolution (ground pixel size) of the radar image along the line parallel to the sensor's motion
----------------------	----------	---	--

2.1 SAR Geometry

The geometrical characteristics of radar imagery differ from standard image geometry (Lin et Fuh 1998; Turner et al. 2021).

60 In the case of radar imagery, some parameters need to be defined and distinguished when applied to satellite and aerial InSAR or to GB-InSAR. The abbreviations are summarized in Table 1.

2.1.1 LoS, azimuthal and range directions

In the case of aerial radar, the azimuthal direction corresponds to the direction of the displacement of the aircraft or satellite; the range direction, or look direction is the direction perpendicular to the azimuthal direction. The direction of the radar-to-
65 target line is the LoS direction whose distance is called range or LoS distance (dLoS). It varies from near-range, for the line forming the smaller angle with the vertical radar-Earth line (nadir), to the far-range for the direction with the larger angle (Figure 1a).

In the case of the GB-InSAR, the azimuthal and range directions are parallel and perpendicular to the rail, respectively. dLoS definition is similar to the aerial radar case but the near-range is the line forming the smaller angle with the horizontal line and
70 the fare-range the larger angle (Figure 1b).

2.1.2 Look angle or off-nadir angle Φ , incident angle θ and depression angle γ

Look angle or off-nadir angle Φ , incident angle θ and depression angle γ are well-defined in the case of satellite imagery when the monitored surface is assumed to be sub-horizontal. The look angle Φ is the angle between the vertical line and the LoS. The depression angle γ is the complement angle of the look angle. The definition of the incident angle θ is the same as in
75 optical geometry, i.e. the angle between the LoS and the normal to the monitored surface (Figure 2a, b). To simplify, when the monitored surface is horizontal for satellite InSAR or vertical for GB-InSAR, both θ and Φ are the angle between the LoS and the normal to the observed surface and are thus assumed to be equal.

2.1.3 Antenna beamwidth ε

The emitted signal propagates within a certain emission cone defined by an angle called beamwidth ε (Woodhouse, 2006; Miron, 2006) which is proportional to the wavelength according to diffraction laws (Lipson et al. 1995) and defines the maximum extent of the illuminated area. The radar footprint on the ground is an ellipsoid (Figure 1a, b). Radar manufacturers provide antenna emission characteristics that are displayed in the form of a polar diagram (Toomay and Hannen, 2004). In the case of GB-InSAR, the vertical beamwidth ε_v is limited to 30° to avoid interferences with other radar devices such as planes (Anon, 2017: « ETSI EN 300 440 v2.1.1 ») while the horizontal beamwidth ε_h is not legislatively restricted (Figure 1d).

85 **2.1.4 Radar bandwidth BW, satellite radar pulse length τ_{FMPR} and GB-InSAR sweep length τ_{FMCW}**

One of the major differences between GB- and satellite InSAR is related to their emitted signal. In the case of satellite InSAR, the transmitted signal must have sufficient amplitude to reach the Earth's surface and be backscattered with enough intensity to be detected by the radar receiver (Ferretti et al. 2014). However, the antennas are not able to continuously generate and send such a high-peak power signal. To overcome this technical limitation, the satellite radar signal is sent by pulses defined by a certain pulse duration τ_{FMPR} comprised between 10 and 100 μs depending on the satellite (Figure 1d). The emitted signal frequency is modulated to perform a pulse compression or chirping (Klauder et al., 1960; Hein, 2004). Such a radar can be named Frequency Modulated Pulsed Radar (FMPR). The satellite radar bandwidth BW (Figure 1g) is the difference between the maximal and minimal emitted frequency. The time between two consecutive pulses is called Pulse Repetition Interval (PRI) and the duration of the emission of one pulse is the pulse length τ_{FMPR} .

95 The European Telecommunications Standards Institute (ETSI) defined some standards regarding the Short-Range Devices (SRD) emitting radio signals (Anon, 2017). The power and the frequencies of signals sent by terrestrial radar are limited to not interfere with other devices emitting and receiving radio signals. Specifically, for GB-InSAR operating in the frequency range of 17.1 to 17.3 GHz, the maximum limits for the frequency bandwidth and the power output are 200 MHz and 26 dBm, respectively.

100 GB-InSAR is considered as a Frequency Modulated Continuous Wave radar (FMCW radar, Wolff 1998; Nadav 2003), the signal emitted is of lower intensity compared to satellite radar emissions. Since the signal is continuously emitted, one is lacking the timing mark necessary to isolate the backscattered signals and discriminate the range. This is achieved instead by modulating the frequency sent by the transmitter (Figure 1f). The GB-InSAR bandwidth (BW, Figure 1h) is the difference between the upper and lower cut-off frequencies. The duration of one sequence of frequency variation is the sweep length τ_{FMCW} .

BW in the case of satellites is generally smaller than for GB-InSAR, ranging between 10 MHz and 80 MHz, and between 70 MHz and 200 MHz, respectively.

2.1.5 Real Antenna length L_{real} and synthetic antenna length L

110 The azimuthal resolution is inversely proportional to the real antenna length L_{real} for RAR acquisition. In the case of SAR acquisition, a synthetic aperture antennas L is used to increase this resolution. For a GB-InSAR installed on a rail, the antenna length L corresponds to the rail length used to focus the radar image, which is in practice slightly shorter than the total rail length.

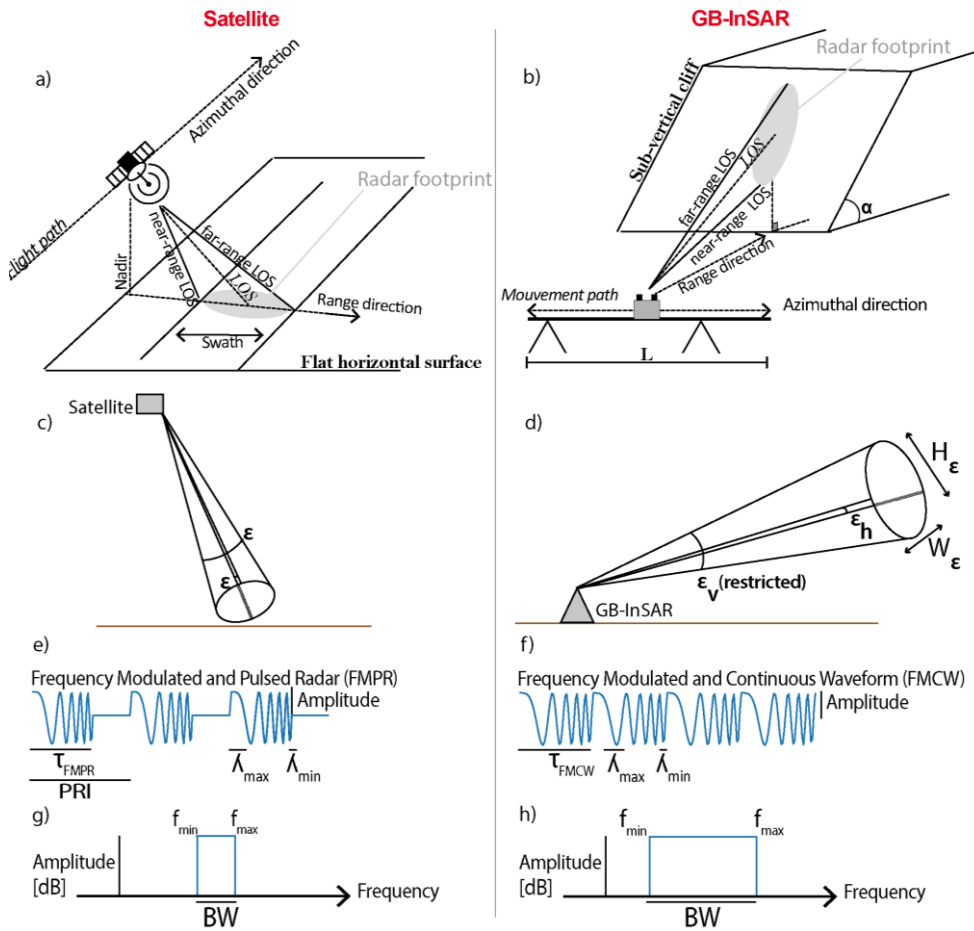
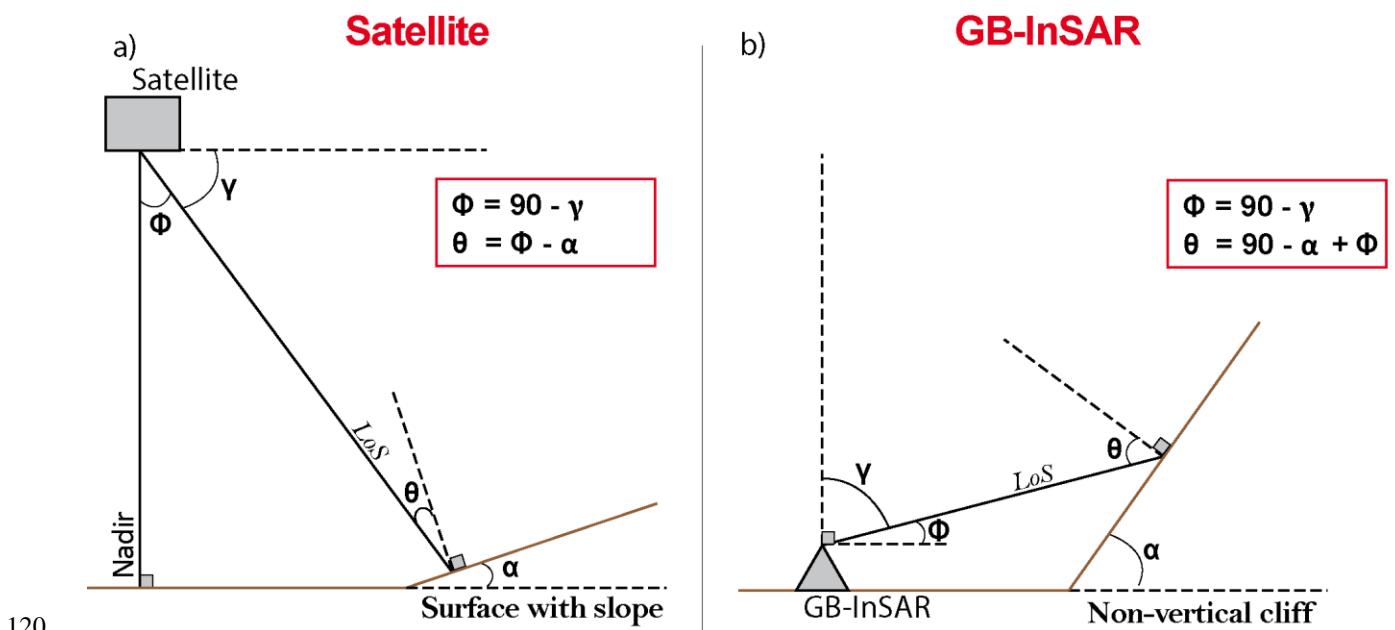


Figure 1 : Illustration and comparison of radar acquisition characteristics in the case of satellite InSAR (Left) and GB-InSAR (Right). (a), (b) Geometry of the acquisition defining the azimuthal and range directions. (c), (d) Beamwidth characteristics. (e), (f) Waveform characteristics. (g), (h) Frequencies characteristics.



120

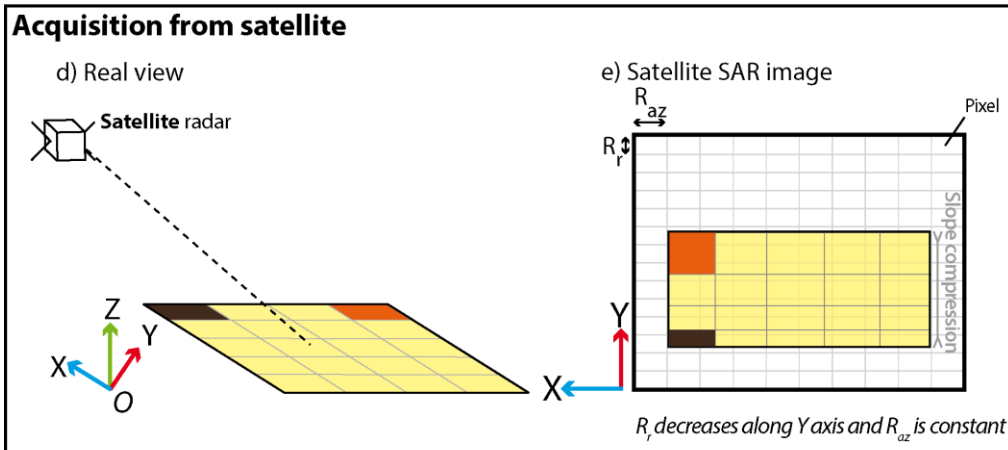
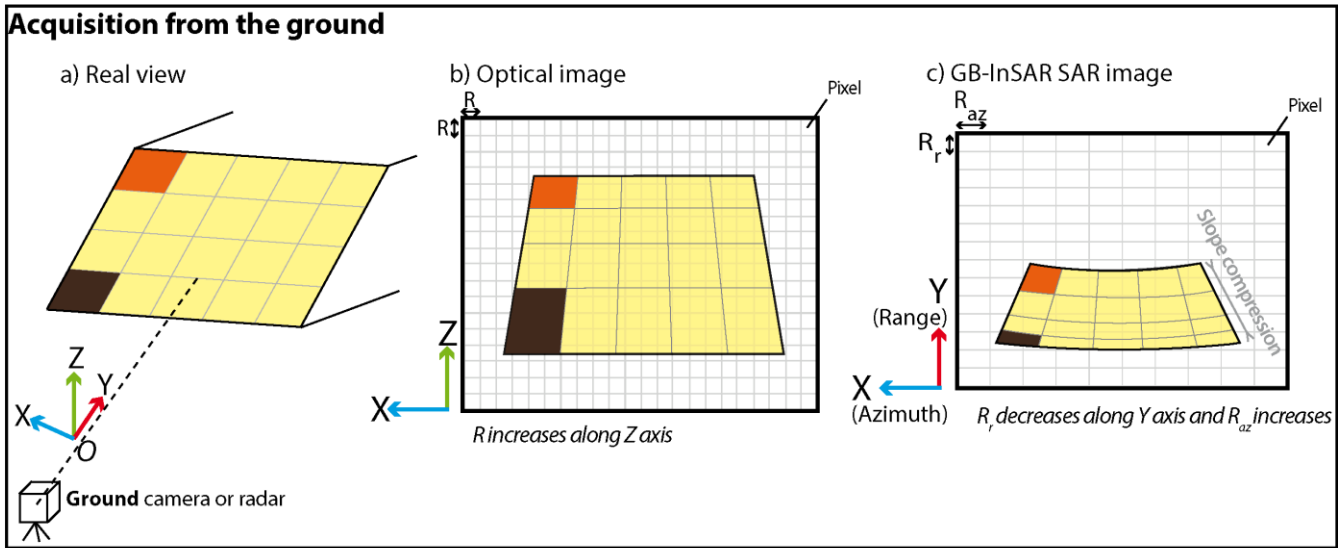
Figure 2 : Illustration of the main specific angles used when describing a SAR acquisition. (a) Case of satellite radar acquisition. (b) Case of GB-InSAR acquisition.

2.2 Spatial resolution

2.2.1 Radar and optical images

125 When representing the world (Figure 3a,d) by an image, one must distinguish the radar image from the optical image, which is the visual display we are commonly used to (Figure 3b). The radar image is based on the distance between the radar antenna and each feature of the scene: the bottom line of the image corresponds to the monitored surface closest to the radar. Additionally, in radar geometry, range and azimuthal resolutions are defined differently and by default, pixels are not square (Figure 3c, e).

130



135 **Figure 3 : Comparison of the view of a surface. a) Real view in a parallel projection with the camera or radar acquiring the image from the ground, b) Optical image taken with a camera from the ground. R_r increases with Z . Consequently, the distance between two consecutive horizontal lines decreases along Z , c) GB-InSAR SAR image (after Tapete et al., 2013). R_{az} increases and R_r decreases along Y . Consequently, the distance between two consecutive horizontal lines increases along Z . d) Real view in a parallel projection with the satellite radar acquiring the image from the satellite orbit. e) Satellite SAR image. R_{az} is constant along Y while R_r decreases. Consequently, the distance between two consecutive horizontal lines increases along Y . In the case of the radar images (c, e), the slope is compressed compared to the optical image, due to the foreshortening effect.**

140 **2.2.2 Azimuthal resolution R_{az}**

The azimuthal resolution R_{az} corresponds to the resolution parallel to the flying trajectory in the case of satellite InSAR or parallel to the rail in the case of a Linear GB-InSAR, or the horizontal resolution in the radar image. Its value differs between satellite InSAR and GB-InSAR.

The synthetic antenna aperture length being constrained by the rail length for the GB-InSAR, R_{az} is related to the radar
 145 beamwidth (itself related to the wavelength λ), the range distance dLoS and the synthetic antenna length L with the following
 relation (Henderson and Lewis, 1998; Jensen, 2006):

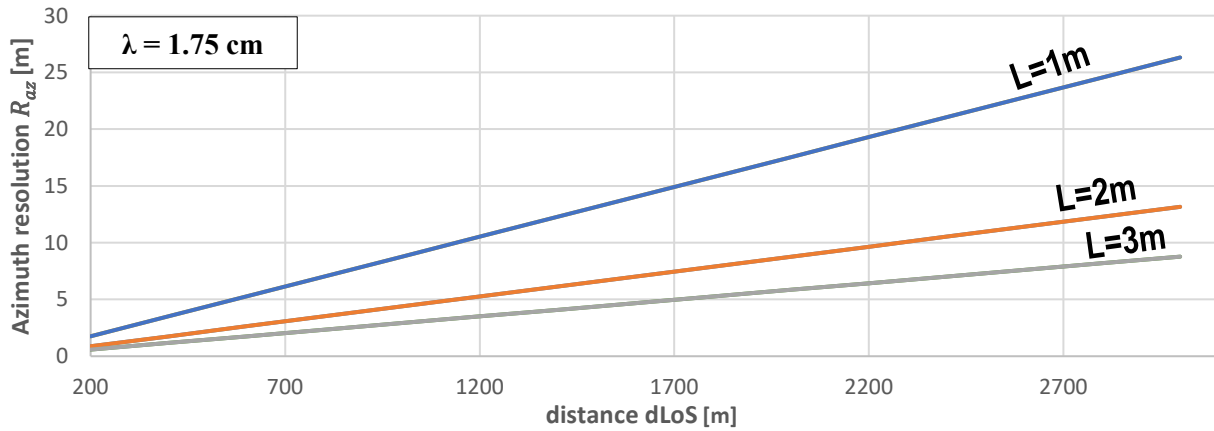
$$R_{az,GB-InSAR} = \frac{dLoS \lambda}{2L} \quad (1)$$

Thus, R_{az} increases from near- to far-range and the GB-InSAR image of a slope is a cone (Figure 3d). Conversely, for satellite
 the synthetic aperture length L can be infinite, R_{az} is dLOS-free and λ -free (Henderson and Lewis, 1998) and defined as:

150
$$R_{az,satellite} = \frac{L_{real}}{2}. \quad (2)$$

The satellite InSAR image of a slope is thus rectangular (Figure 3c).

Figure 4 presents the influence of dLoS and L on the azimuthal resolution in the case of the GB-InSAR.



155 **Figure 4 : Influence of the rail length used to focus the GB-InSAR image corresponding to the synthetic antenna length L and the distance dLoS on the azimuthal resolution R_{az} , for a Ku-band with a wavelength equal to λ 1.75 cm. The longer the rail length, the better the azimuthal resolution.**

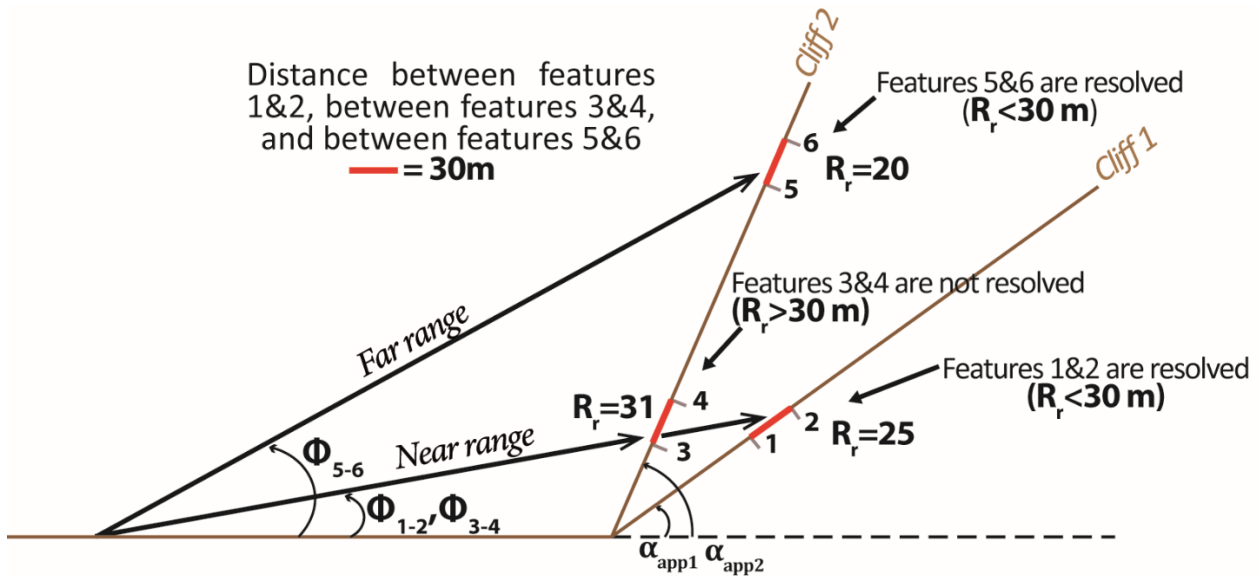
2.2.3 Ground range resolution R_r

The ground range resolution R_r is the resolution along the LoS direction or the vertical resolution. It corresponds to the
 160 minimum time needed to distinguish two consecutive pulses (Woodhouse, 2006). It is ground-geometry dependent, linked to
 the incidence angle θ , the speed of light c and the pulse length τ_{FMPR} (after pulse compression) or sweep length τ_{FMCW}
 according to the following relations (Henderson and Lewis, 1998; Jensen, 2006; Mahafza, 2000; McCandless and Jackson,
 2004):

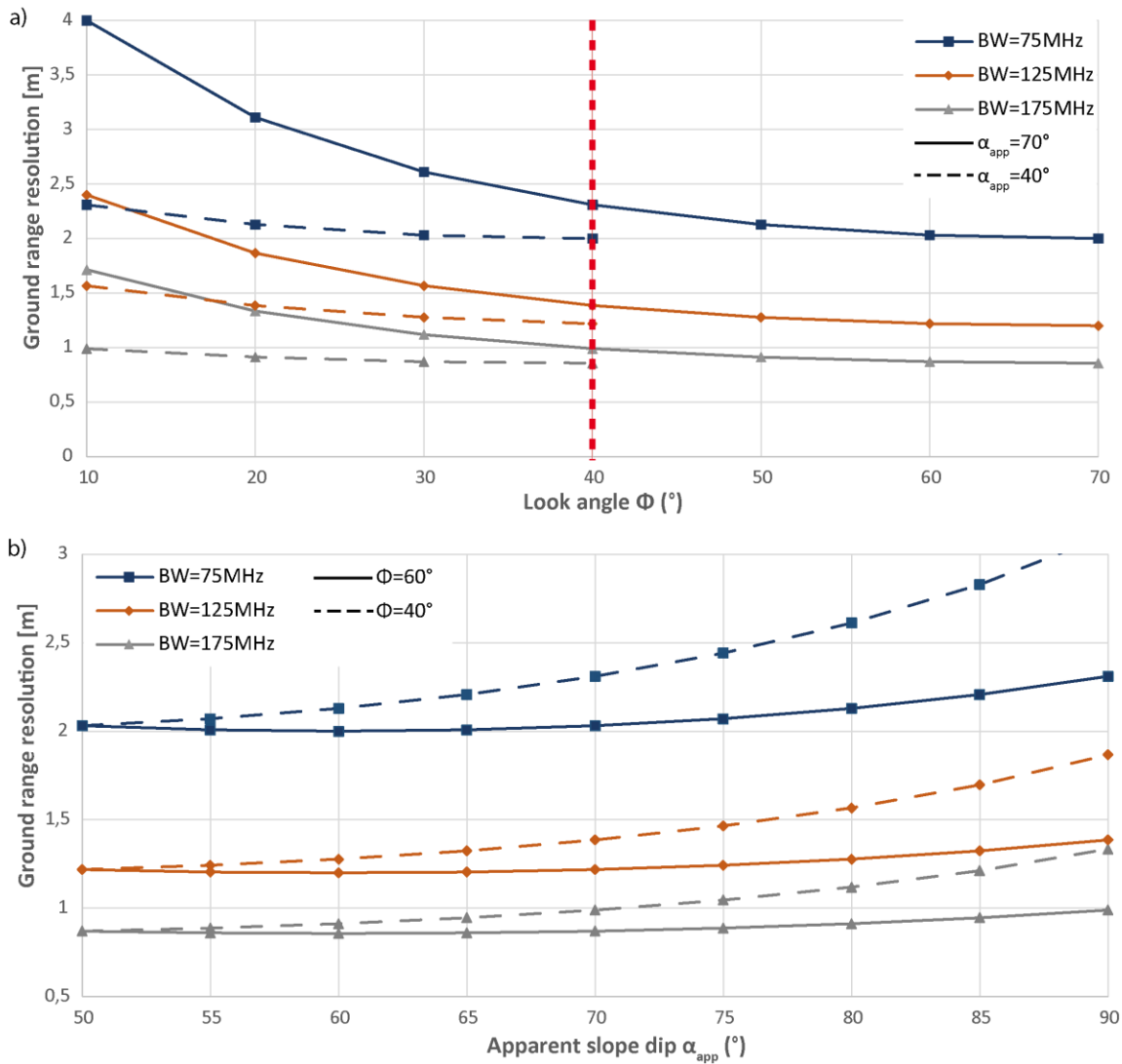
$$R_{r,satellite} = \frac{\tau_{FMPR} c}{2 \sin \theta} = \frac{c}{2 BW \sin \theta} = \frac{c}{2 BW \sin(\Phi - \alpha_{app})} \quad (3)$$

165
$$R_{r,GB-InSAR} = \frac{\tau_{FMCW} c}{2 \sin \theta} = \frac{c}{2 BW \sin \theta} = \frac{c}{2 BW \sin(90 - \alpha_{app} + \Phi)} = \frac{c}{2 BW \cos(\Phi - \alpha_{app})} \quad (4)$$

170 The monitored cliff geometry has an impact on the range resolution with two major consequences according to Equation 4:
 (1) Near-range surfaces and features possess, along a planar topography, less resolution in range than those in the far-range because Φ increases with the range and (2) steeper slopes increase the range resolution by increasing α_{app} (Figure 5, Sabins 1997; Stimson 1998; Jensen 2006). Furthermore, the shorter the pulse length τ_{FMPR} or sweep length τ_{FMCW} , the finer the resolution. Nevertheless, one must be careful in the choice of the pulse length because if a short τ_{FMPR} or τ_{FMCW} results in a better resolution, the backscatterer signal is also weaker and might not be detected if too low. For GB-InSAR, the parameter that can be chosen by the user is the bandwidth BW. The further away the radar is installed from the target area, the smaller should be the bandwidth to be sure to detect the backscattered signal. A good balance between an acceptable resolution and a sufficiently strong backscattered signal must be found (Figure 6a, b).



175 Figure 5 : Ground range resolution R_r for two different slope angles and two different depression angles (adapted from Sabins 1997). The distance between features 1&2, features 3&4 and features 5&6 is the same, 30 cm. However, features 1 and 2, located on a gentle slope and at a near-range distance from the GB-InSAR, are resolved ($R_r = 25$ m) as well as features 5 and 6 located at a far-range distance and on a steep slope ($R_r = 20$ m), while features 3 and 4 located on the same steep slope as features 5 and 6 but at a
 180 near-range distance, are not resolved ($R_r = 31$ m).



185 **Figure 6 : Influence of some GB-InSAR parameters on the range resolution R_r . a) Influence of the look angle Φ for different BWs. It is interesting to notice that the resolution varies little when Φ is larger than 40° . b) Influence of the apparent slope dip α_{app} for different BWs.**

2.2.4 Number of pixels and slope compression

During a monitoring campaign, the surveyor focuses on a Slope of Interest (SoI). A monitoring campaign is effective when information concerning this SoI is distributed across a wide range of pixels rather than compressed within a few; this involves attempting to get the finest possible range resolution. The position of the GB-InSAR will have an influence on the resolution and the number of pixels in which the SoI will be contained can be estimated with the formula:

190

$$Nb_{pixelRange} = \frac{D_{SoI}}{R_r}, \quad (5)$$

where D_{SoI} is the distance along the monitored slope of the SoI.

The steeper the slope, the more the information will be compressed, and some interesting features may be contained in the same pixel. Given this consideration, if one has the choice between two radar installations, it is worth (1) reducing the range distance (Figure 7a) and (2) reducing the apparent slope angle α_{app} of the measured cliff to increase the apparent SoI distance (Figure 7b). The apparent slope angle can be reduced by placing the radar aside instead of in front of the measured slope and by applying the Equations (Addie, 1968):

$$\alpha_{app} = \tan^{-1}(\tan \alpha \times \sin \omega) \quad (6)$$

$$\omega = \omega_{LOS} - \omega_{slope}, \quad (7)$$

with ω the angle between the slope direction and the LoS direction, and ω_{LOS} and ω_{slope} being the orientation of the LoS toward north and the slope strike, respectively. Table 2 lists the advantages and drawbacks of each radar position.

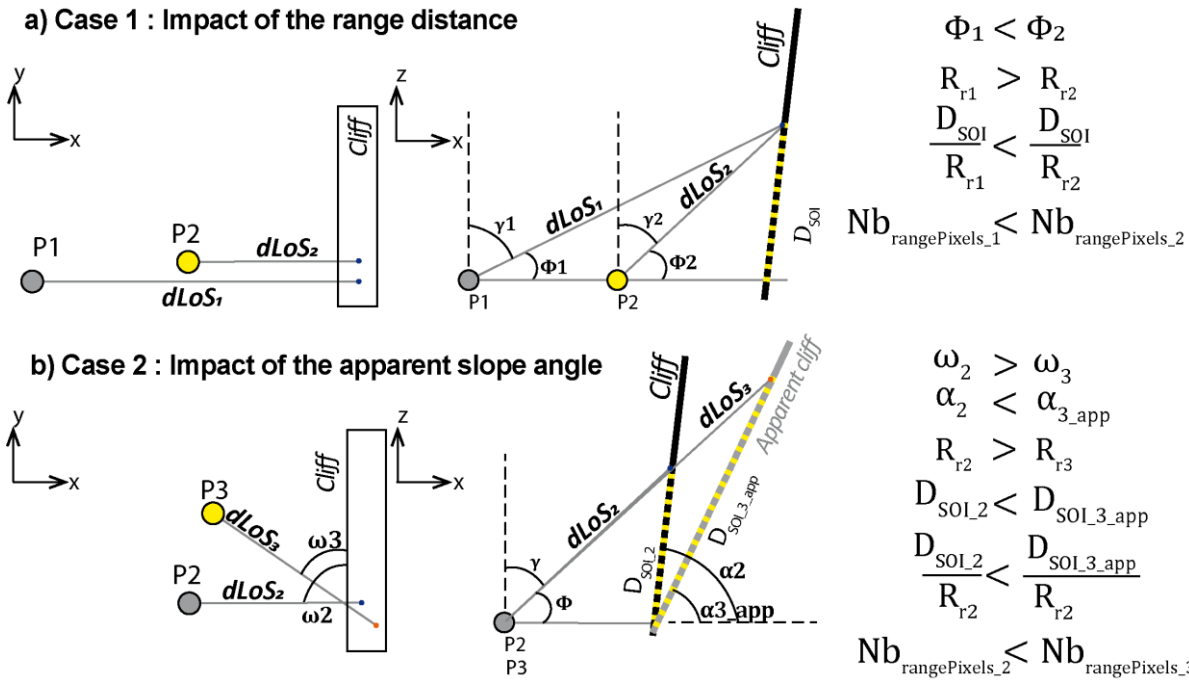


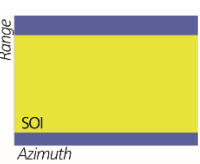


Figure 7 : Two scenarios of selection of the best GB-InSAR installation to get the less compression of the SoI in range. The best location is highlighted in yellow. a) Case 1: Installation near VS far from the monitored cliff. b) Case 2: Installation in front of VS from aside the monitored cliff. When looking aside, α_{app} is smaller according to Equation 6 and the apparent SoI length on slope in the radar direction is longer so the information is distributed in more pixels in range.

Table 2 : Advantages and drawbacks of each position presented in Figure 7.

POINT	Location	Advantages	Drawbacks	Resulting radar image
P1	<ul style="list-style-type: none"> Range direction perpendicular to cliff strike Long range distance 	Large illuminated area Dslope.	Poor range resolution, Compression of information in range. Important features may not be resolved.	
P2	<ul style="list-style-type: none"> Range direction perpendicular to cliff strike Short range distance 	Good range resolution, Important features can be distinguished.	Small illuminated area Dslope, Potentially more shadowing than with P1.	
P3	<ul style="list-style-type: none"> Range direction not perpendicular to cliff strike (Decrease apparent slope) Short range distance 	Smaller apparent dip and greater range resolution compared to P2.	Some important features can be in shadow, LoS may not be parallel to the displacement, the recorded displacement value may be less than the real one, assuming a displacement along the steepest slope.	

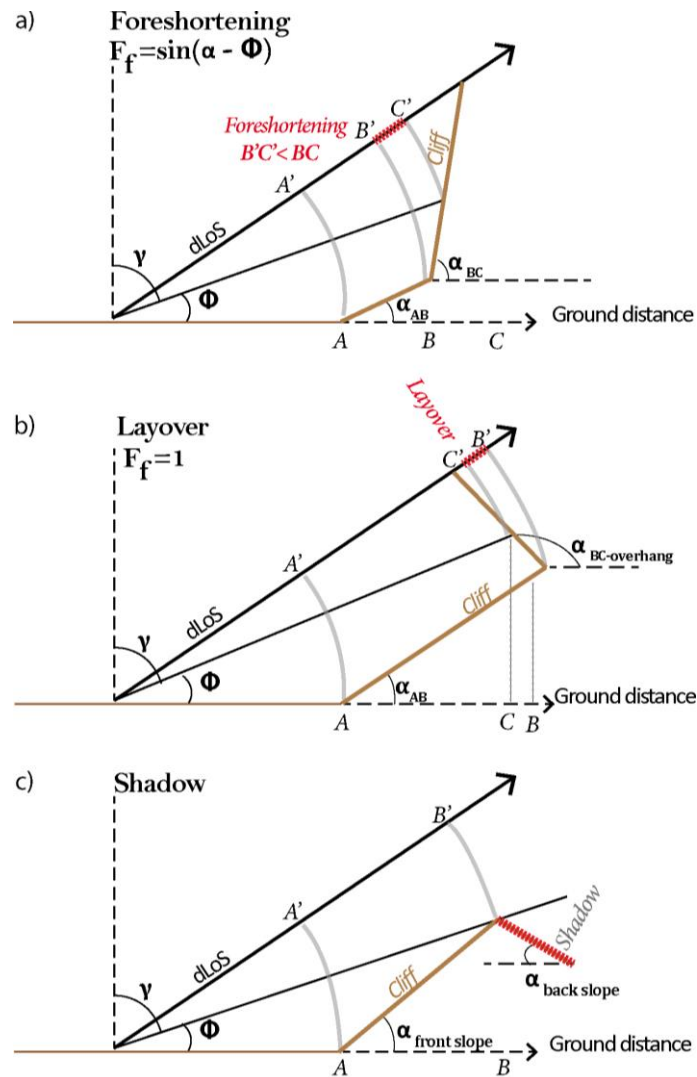
2.3 Shadow, foreshortening and layover

215 Three geometrical notions must be reminded about radar geometry, because they can trigger noise and/or loss of information (Jensen, 2006):

- *Foreshortening*: Any terrain with a slope α inclined toward the radar (foreslope) result in a compression and a brightening of its surface in the radar image, also called foreshortening. Conversely, slopes inclined away from the radar (backslope) appear darker and elongated in the image (Figure 8a). The foreshortening factor F_f can be defined as:

220
$$F_f = \sin(\alpha - \Phi) \quad (8)$$

- *Layover*: If the foreslope angle is greater than the look angle Φ , one can observe layover. The backscatter signal of the layover object will reach the radar receiver before the backscatter signal of the object located before. The information contained in the signal will be stored in the previous pixel in range of the image resulting in a layover distortion of the image which cannot be corrected. With a GB-InSAR, layover effects occur in the case of an overhanging wall (Figure 8b).
 - *Shadow*: An area hidden by a slope or by any other feature is not illuminated by the radar and will not be seen in the radar image, resulting in a loss of information. This can be for instance a deep valley or the ground behind a tall building (Figure 8c).
- 225



230 **Figure 8 : Illustration of geometrical artefacts in the case of GB-InSAR. a) Foreshortening, b) Layover, c) Shadow effects.**

3 Methodology

3.1 GB-InSAR constrains

Caduff et al. (2015) presents in a review a list of points to carefully consider when choosing the location for the GB-InSAR installation, including the visibility of the target area, the SoI, the foreshortening effects, the expected displacement (rate, direction, mechanism), the atmospheric influences and the technical constraints (hardware, setup, accessibility, ...).

The MATLAB tool presented here is aimed at estimating some of those parameters and choosing the best location when several options are possible. The constrains estimated with the tool are the following:

- Range distance dLoS. The bandwidth BW must be adjusted based on this distance and in any case the target should not be further away by more than 4 or 5 km, depending on the GB-InSAR device, to avoid the risk of a too weak backscatter signal amplitude.
- Resolution in range and in azimuth. Once the potential location is found, it is worth estimating the resolution that will be obtained, as well as the extend of the surface illuminated by the radar.
- Areas in shadow and those subject to a strong foreshortening.

3.2 Input parameters

3.2.1 The DEM

The MATLAB tool requires as first input a Digital Elevation Model (DEM) in an ascii format, cropped around the area of interest. The MATLAB code converts it into a 3D point cloud, which is displayed in a window. For the use that will be made of the DEM, a resolution of 5 m is sufficient. For each pixel of the grid, the dip and dip direction is calculated with the function “gradient” (MATLAB, 2023). Additionally, the user provides the coordinates of the center of the area of interest and of the location where he considers installing the radar.

3.2.2 Radar parameters

The parameters that will be estimated are related to the radar characteristics described above (L, BW and ϵ) and must be set up by the user before starting the computation because they influence the resulting resolution as well as the extent of the illuminated area. Since the vertical beamwidth is limited in the case of the GB-InSAR, vertical and horizontal beamwidth are respectively selected by the user and denoted ϵ_v and ϵ_h .

3.3 Estimation of output radar results

3.3.1 Foreslope and distance maps

Firstly, when installing the radar, the distance between the radar and the target surface must be estimated to not be greater than 4 or 5 km. Once the location of the radar ($x_{radar}, y_{radar}, z_{radar}$) is provided, a map is displayed giving for each point of coordinates ($x_{target}, y_{target}, z_{target}$) its distance to the radar defined by:

$$distance = \sqrt{\Delta x^2 + \Delta y^2 + \Delta z^2}, \quad (9)$$

with $\Delta x = x_{target} - x_{radar}$, $\Delta y = y_{target} - y_{radar}$, $\Delta z = z_{target} - z_{radar}$. Slopes facing the radar -or foreslope- can result in foreshortening effect whereas slopes facing away -or backslope- will always be in shadow. That information is displayed in a second map, where the foreslope points have a 1 value and the other points the value -1. To produce this map, the apparent dip α_{app} is computed for each point with Equation 6. The fore – and backslopes are deduced from α_{app} as is:

$$\begin{aligned} \text{If } \alpha_{app} > 0 &\rightarrow \text{Foreslope} \\ \text{If } \alpha_{app} < 0 &\rightarrow \text{Backslope} \quad (10) \end{aligned}$$

3.3.2 Radar footprint and illuminated area estimation

The radar footprint is an ellipse, within which the user selects a smaller area where to focus the radar acquisition. This illuminated surface is selected by choosing the minimum and maximum azimuth Az°_{\min} and Az°_{\max} and the minimum and maximum range R_{\min} and R_{\max} of the acquisition and should encompass the whole instable area to monitor, as well as an area supposed to be stable for the atmospheric corrections (Pipia et al., 2008; Noferini et al., 2005) and the post-processing unwrapping (Goldstein et al., 1988).

Before installing the radar and starting the acquisition, it is worth checking the maximum possible radar footprint as well as the illuminated surface according to the batch of azimuths and ranges selected by the user.

Once the radar and the target location are selected, the map is updated to display the footprint and the points illuminated by the radar during the acquisition according to the parameters R_{\min} , R_{\max} , Az°_{\min} and Az°_{\max} selected by the user.

To do so, the coordinates of each point of the point cloud are converted from the global geographical coordinate system *global* in a local coordinate system *local* whose frame origin is the center of the region of interest selected by the user. The X axis is horizontal and perpendicular to the LoS direction, and the horizontal Y axis is perpendicular to X. Z axis is a vertical unit vector. Thus, the unit vectors of the *local* frame are:

$$\begin{pmatrix} X_{unit} \\ Y_{unit} \\ Z_{unit} \end{pmatrix}_{local} = \begin{pmatrix} \frac{\Delta y_{global}}{\sqrt{\Delta y_{global}^2 + \Delta x_{global}^2}} & \frac{\Delta x_{global}}{\sqrt{\Delta y_{global}^2 + \Delta x_{global}^2}} & 0 \\ \frac{\Delta x_{global}}{\sqrt{\Delta y_{global}^2 + \Delta x_{global}^2}} & \frac{\Delta y_{global}}{\sqrt{\Delta y_{global}^2 + \Delta x_{global}^2}} & 0 \\ 0 & 0 & 1 \end{pmatrix}. \quad (11)$$

Each point coordinates can be converted from the *global* geographical coordinate system to the new *local* coordinate system

by applying a translation \mathbf{T} defined by the vector $\overrightarrow{LoS} \begin{pmatrix} \Delta x_{global} \\ \Delta y_{global} \\ \Delta z_{global} \end{pmatrix}$ followed by a rotation of matrix $\mathbf{\Omega}$:

$$\begin{cases} \mathbf{T} = \begin{pmatrix} \Delta x_{global} \\ \Delta y_{global} \\ \Delta z_{global} \end{pmatrix} \\ \mathbf{\Omega} = \begin{pmatrix} a & -b & 0 \\ b & a & 0 \\ 0 & 0 & 1 \end{pmatrix} \end{cases}. \quad (12)$$

The relation linking the coordinates of each point in the *global* geographical coordinate system and the new *local* coordinate system is:

$$\begin{pmatrix} x \\ y \\ z \end{pmatrix}_{local} = \mathbf{\Omega} \cdot \begin{pmatrix} x \\ y \\ z \end{pmatrix}_{global} + \mathbf{T} \quad (13)$$

$$\begin{pmatrix} x \\ y \\ z \end{pmatrix}_{local} = \underbrace{\begin{pmatrix} a & -b & 0 \\ b & a & 0 \\ 0 & 0 & 1 \end{pmatrix}}_{rotation\ matrix} \cdot \begin{pmatrix} x \\ y \\ z \end{pmatrix}_{global} + \underbrace{\begin{pmatrix} \Delta x_{global} \\ \Delta y_{global} \\ \Delta z_{global} \end{pmatrix}}_{translation\ matrix}. \quad (14)$$

290 The couple of values (a, b) is found by solving the system with the coordinates of the target point $\begin{pmatrix} 0 \\ 0 \\ 0 \end{pmatrix}_{local}$ in the local coordinate system:

$$\begin{pmatrix} 0 \\ 0 \\ 0 \end{pmatrix}_{local} = \begin{pmatrix} a & -b & 0 \\ b & a & 0 \\ 0 & 0 & 1 \end{pmatrix} \cdot \begin{pmatrix} x_{target} \\ y_{target} \\ z_{target} \end{pmatrix}_{global} + \begin{pmatrix} \Delta x_{global} \\ \Delta y_{global} \\ \Delta z_{global} \end{pmatrix} \quad (15)$$

All points of the point cloud are converted into the new local coordinate system with Equation 13. It is then possible to filter points that belong to the radar footprint, knowing ε_v and ε_h (Figure 9a). A point $P(x_{local}, y_{local}, z_{local})$ is within the footprint if:

295
$$|z_{local}| < \sqrt{H_\varepsilon^2 - \left(\frac{x_{local}}{L_\varepsilon}\right)^2}, \quad (16)$$

with:

$$L_\varepsilon = dLoS(O) * \tan \varepsilon_h \quad (17)$$

$$H_\varepsilon = dLoS(O) * \tan \varepsilon_v. \quad (18)$$

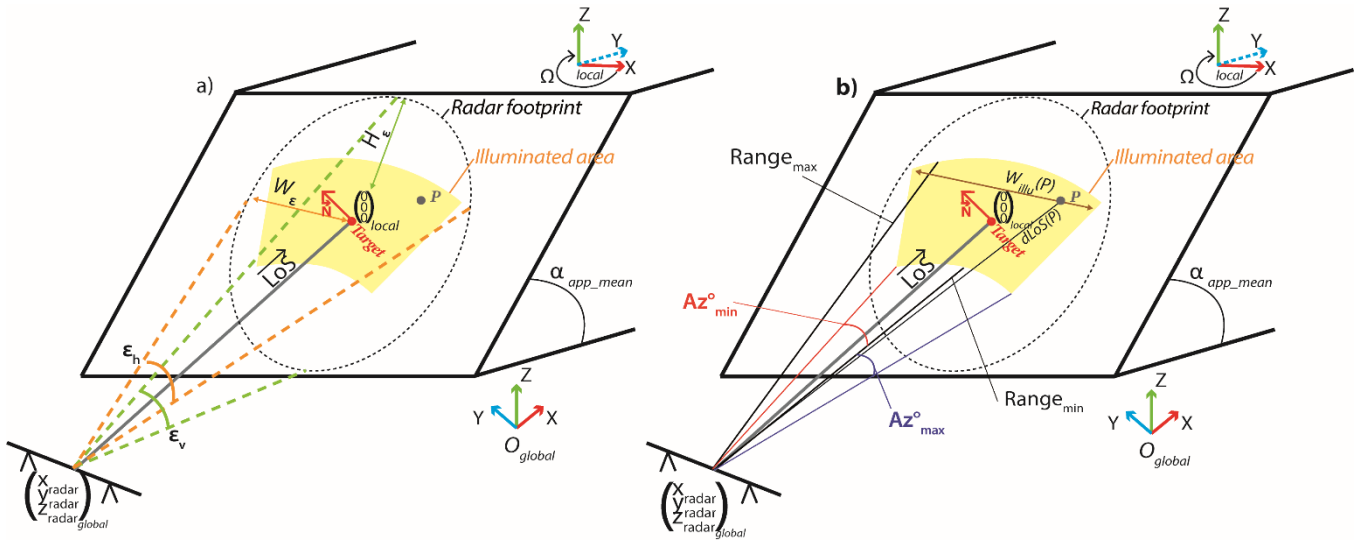
Points belonging to the illuminated area are extracted in a second step. A point $P(x_{local}, y_{local}, z_{local})$ is within the illuminated area if (Figure 9b):

300
$$\begin{cases} P \in \text{footprint} \\ dLoS(P) \in [R_{min}; R_{max}] \\ z_{local} \in [W_{min}(P); W_{max}(P)] \end{cases}, \quad (19)$$

with:

$$\begin{cases} W_{illu_{min}}(P) = dLoS(P) * \tan Az_{min}^\circ \\ W_{illu_{max}}(P) = dLoS(P) * \tan Az_{max}^\circ \end{cases} \quad (20)$$

305 Once the points illuminated by the radar are known, a mean square method (Wolberg, 2006) is used to determine the mean plan intersecting the illuminated points, defined by its normal vector \vec{N} . This vector is then converted into mean slope dip α_{MEAN} and mean slop dip direction ω_{MEAN} .



310 **Figure 9 : Illustration of the change of coordinate frame from a global one $(X, Y, Z)_{global}$ to a local one $(X, Y, Z)_{local}$, centered on the target coordinates, aiming at highlighting the points of the point cloud within the radar footprint and the illuminated area. X_{local} axis is horizontal and perpendicular to LOS , Y_{local} axis is horizontal and perpendicular to X_{local} . a) Point P is within the radar footprint because its coordinates answer the conditions defined in Equation 16. b) Point P is illuminated because its coordinates answer the conditions defined in Equation 19.**

3.3.3 Resolution, foreshortening and layover maps

315 Equations 1 and 4 are applied on each point of the point cloud to estimate the range and azimuthal resolutions and the result is displayed in two distinct maps.

The mean plan dip direction ω_{MEAN} and dip α_{MEAN} being known, the latter is converted in apparent dip from the radar position α_{MEAN_app} , and the foreshortening for this mean plan F_{F_MEAN} is calculated by applying Equation 8, giving a value comprised between $[0;1]$, 0 for no foreshortening and 1 for the beginning of layover. In addition, the foreshortening degree is calculated

320 for each point of the point cloud.

It is then possible to estimate for each point if it will be affected by a stronger or a weaker foreshortening than the mean slope plan by subtracting the mean plan foreshortening F_{F_MEAN} from the foreshortening calculated at each point. Such a map is also one of the outputs of the tool. A negative or positive value implies respectively a weaker or stronger foreshortening at that point than the mean one.

325 3.4 Tool interface

The application coded in MATLAB is presented in a graphical user interface (Figure 10). The user first selects the DEM to import and convert into a 3D point cloud. He gives then the coordinates of the location where he considers installing the radar and the coordinates of the region of interest center. It can be found directly on the point cloud or from a GPS measurement

performed on the field. The radar parameters, listed in Table 3, must also be given before starting the computation. To filter
 330 pixels within the area illuminated during the processing, the user also gives the minimum and maximum ranges and azimuths.
 At the end of the processing, the different maps are displayed in 3D and can be stored in a text file to be reused later.

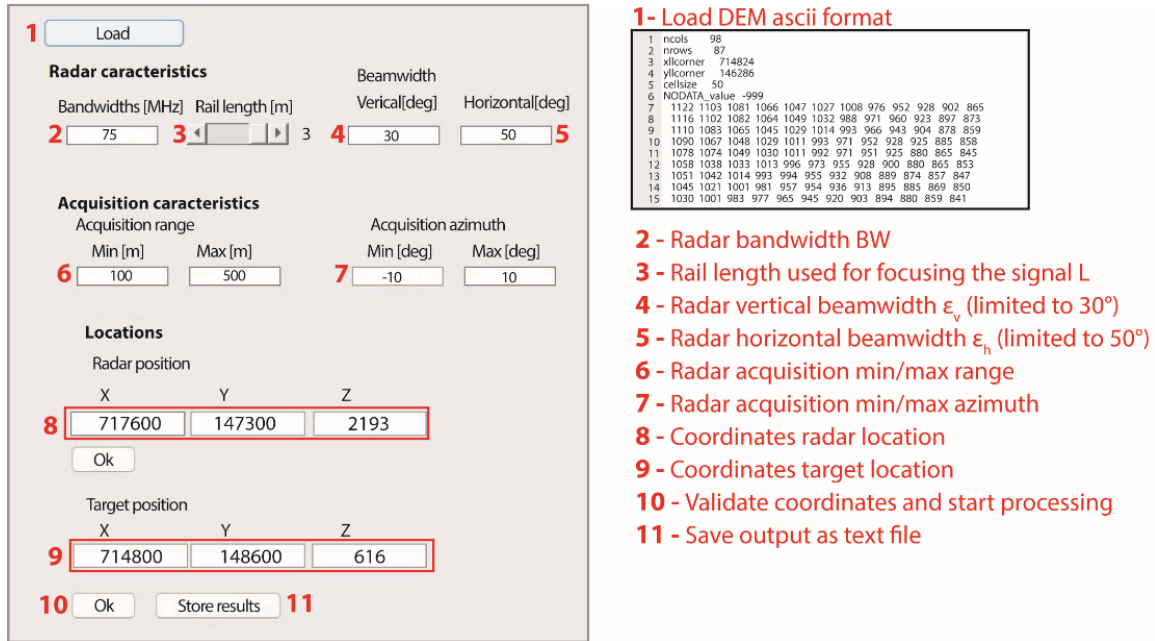


Figure 10 : Interface of the MATLAB tool and the format of the DEM grid to import, in a text file format.

335 4 Description of the tested case studies

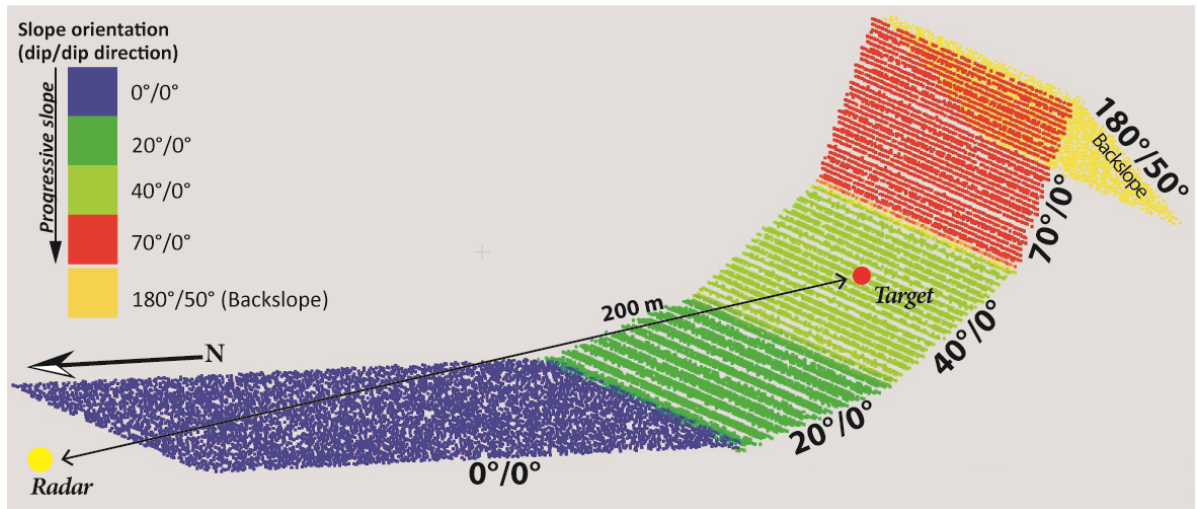
To validate the results obtained with this tool, the later has been tested with a Lisalab GB-InSAR (Table 3) on (1) a simple synthetic cliff created in Cloud Compare, facing north and with a progressive slope and a backslope (Figure 11) and (2) two real cliffs where GB-InSAR monitoring campaigns were conducted (Table 4, Figure 12 and Figure 13).

340 Table 3 : Characteristics of the LiSA GB-InSAR used in this study

Radar system	Rail length L [m]	Antenna type	Maximal horizontal/vertical beamwidth ϵ_h/ϵ_v [°]	Radar band	Central pulse frequency f [GHz]	Bandwidth BW [MHz]	Measurable phenomena max speed [mm/h]
Lisalab	3	Horn antenna	50 ← $\begin{array}{c} 30 \\ \updownarrow \end{array}$ →	Ku-band	17.2	[50-175]	176

Table 4 : The three study cases with their DEM characteristics and the radar parameters chosen

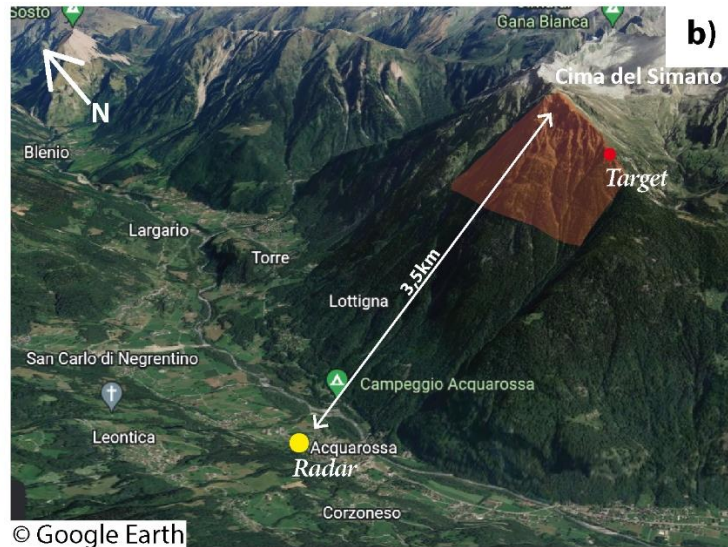
Case study	Geographical coordinate system	Radar location [m]	Target location [m]	Distance estimation [m]	BW [Mhz]	Min/Max Ranges [m]	Min/Max Azimuths [°]
1- Synthetic dataset	-	x – 0 y – 100 z – 1	x – 0 y – -88 z – 20	200	175	180/205	-12/12
2- Cima del Simano	CH1903 LV03	x – 714800 y – 148600 z – 616	x – 717600 y – 147300 z – 2193	3500	75	3100/4200	-9/9
3- La Cornalle	CH1903 LV03	x – 547000 y – 149000 z – 230	x – 548000 y – 150000 z – 685	200	175	140/250	-4/4



345 **Figure 11 : Synthetic dataset: a cliff facing North with a progressive slope dip and a backslope.**

4.1.1 Real case 1: Cima del Simano instability monitoring

Cima del Simano is a deep-seated landslide located in the Ticino canton in Switzerland (Figure 12a). Satellite interferometry measurements highlight the presence of slow sub-vertical gravitational movement on top of the mountain, which motivated the launch of a GB-InSAR monitoring campaign in 2021 (Wolff et al., 2023). A Lisalab GB-InSAR with a 3 m-rail was installed in the valley near a building belonging to the Acquarossa commune to have access to electrical power (Figure 12c).
 350 The acquisition is challenging because the radar is located at its range limit and the top of the cliff, at an altitude of 2500 m, witnesses strong atmospheric effects (Figure 12b).

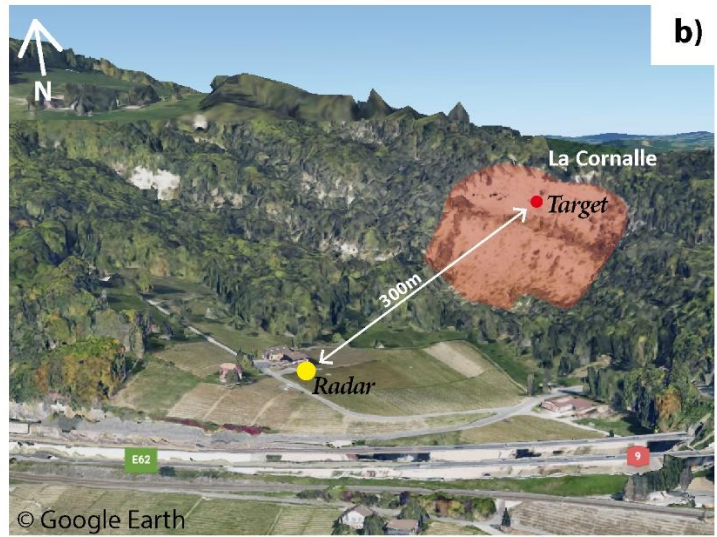
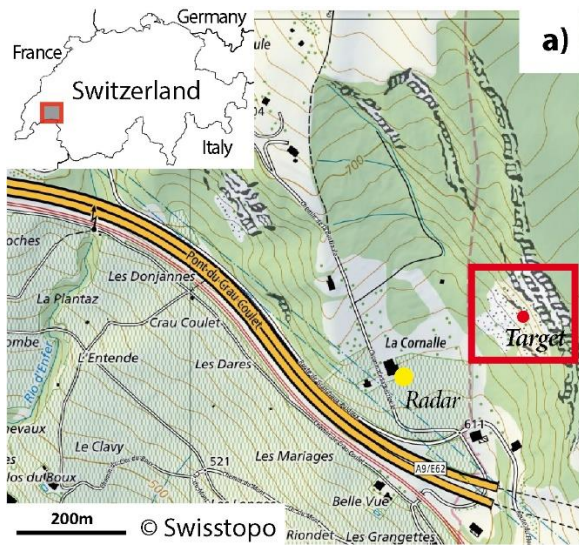


- Measuring head
- Rail
- Pedestrial support on horizontal wall
- Access to electricity
- Power station

355 **Figure 12 : First real studied site: Cima del Simano. a) Location. b) Radar and target location on Google Earth image. c) Lisalab GB-InSAR installation.**

4.1.2 Real case 2: La Cornalle cliff monitoring

La Cornalle cliff located in the Lavaux vineyard (East Lausanne, Switzerland, Figure 13a) is monitored with yearly LiDAR acquisitions since 2013 (Carrea et al., 2014, 2015). This steep cliff is affected by erosion process and frequent rockfall events occur every year (Figure 13b). This site is monitored to estimate the role of the rock surface temperature and of the atmospheric erosion (Fei et al., 2023). In this topic, a GB-InSAR has been installed in August 2022 at the bottom of the cliff. The Lisalab rail has been set up on a flat wall near a vineyard factory to have access to electricity and very near the cliff to get the best possible resolution (Figure 13c).



Measured cliff

Measuring head
Rail

Pedestrial support on horizontal wall

Power station and access to electricity
in the building

365

Figure 13 : Second real studied site: La Cornalle cliff. a) Location. b) Radar and target location on Google Earth image. c) Lisalab GB-InSAR installation.

5 Results

The obtained results are summarized in Table 5 for the three studied cases and some output maps are displayed in Figure 14 in the case of the synthetic dataset, Figure 15 in the case of Cima del Simano and in Figure 16 for La Cornalle cliff. The extra output maps are available in the appendices A to C.

375 **Table 5 : Results obtained with the MATLAB tool for the three study sites.**

Case study	Location	Range resolution [m]	Azimuthal resolution [m]	dLoS [m]	Mean dip	Mean dip direction	Mean foreshortening	Output maps
0	Synthetic dataset	0.95	0.57	200	48°	0°	0.67	Figure 14
1	Cima del Simano	2.0	10.4	3351	51°	344°	0.38	Figure 15
2	La Cornalle	0.92	0.64	267	61°	201°	0.81	Figure 16

5.1.1 Synthetic dataset (Figure 14, Figure A1)

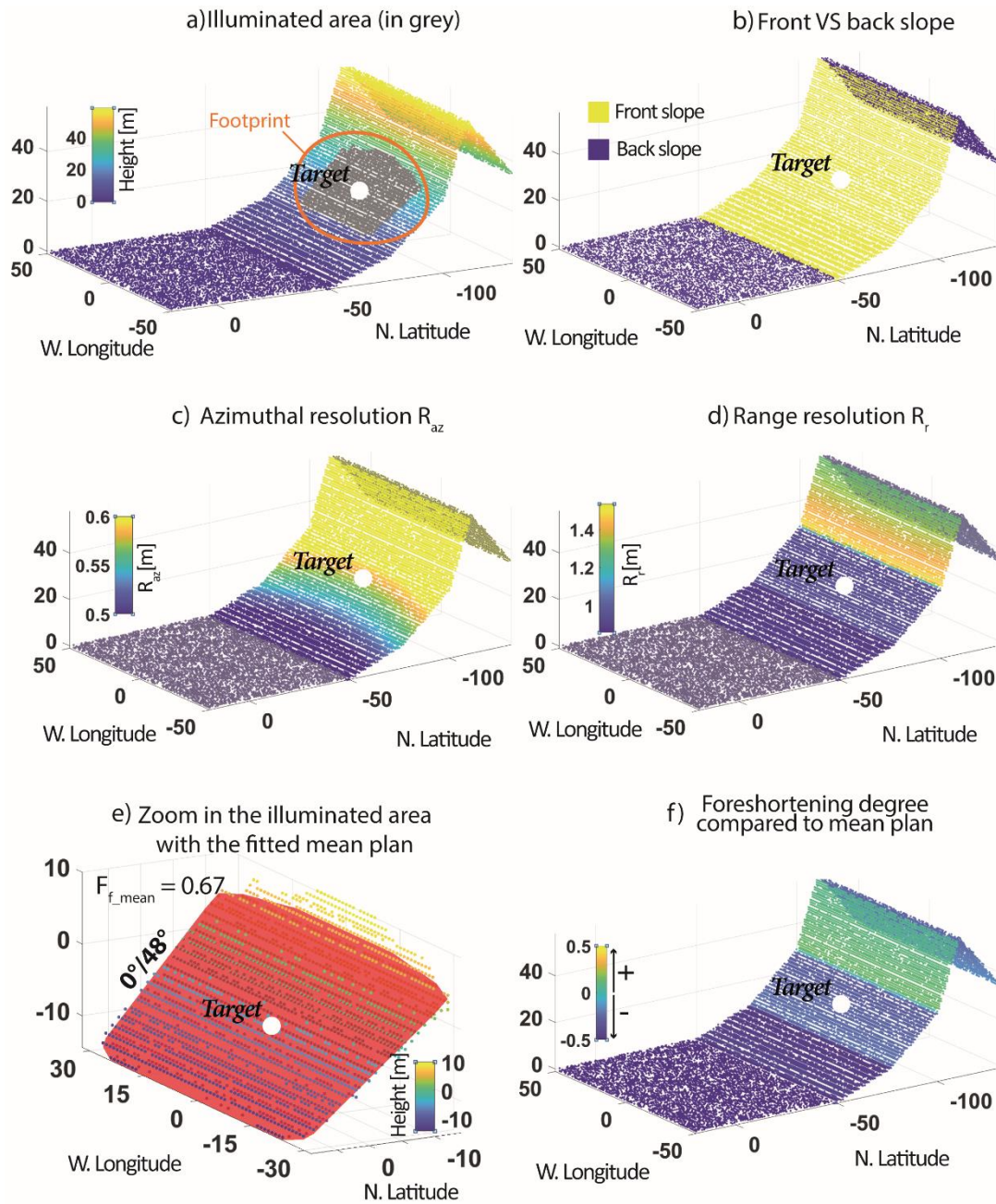
With a LoS distance of 200 m, the range and azimuthal resolutions are respectively 0.95 m and 0.57 m at the target location. The calculated apparent mean dip is 48° because the illuminated area encompasses a major part of the slope with a dip of 40° and a little part of the slope with a dip of 70°. The mean foreshortening of the SoI is 0.67 (Figure 14e) but the points located
380 on the slope with a dip of 40° are less affected by foreshortening than those located on the slope with a dip of 70° (Figure 14f).

5.1.2 Cima del Simano (Figure 15, Figure A2)

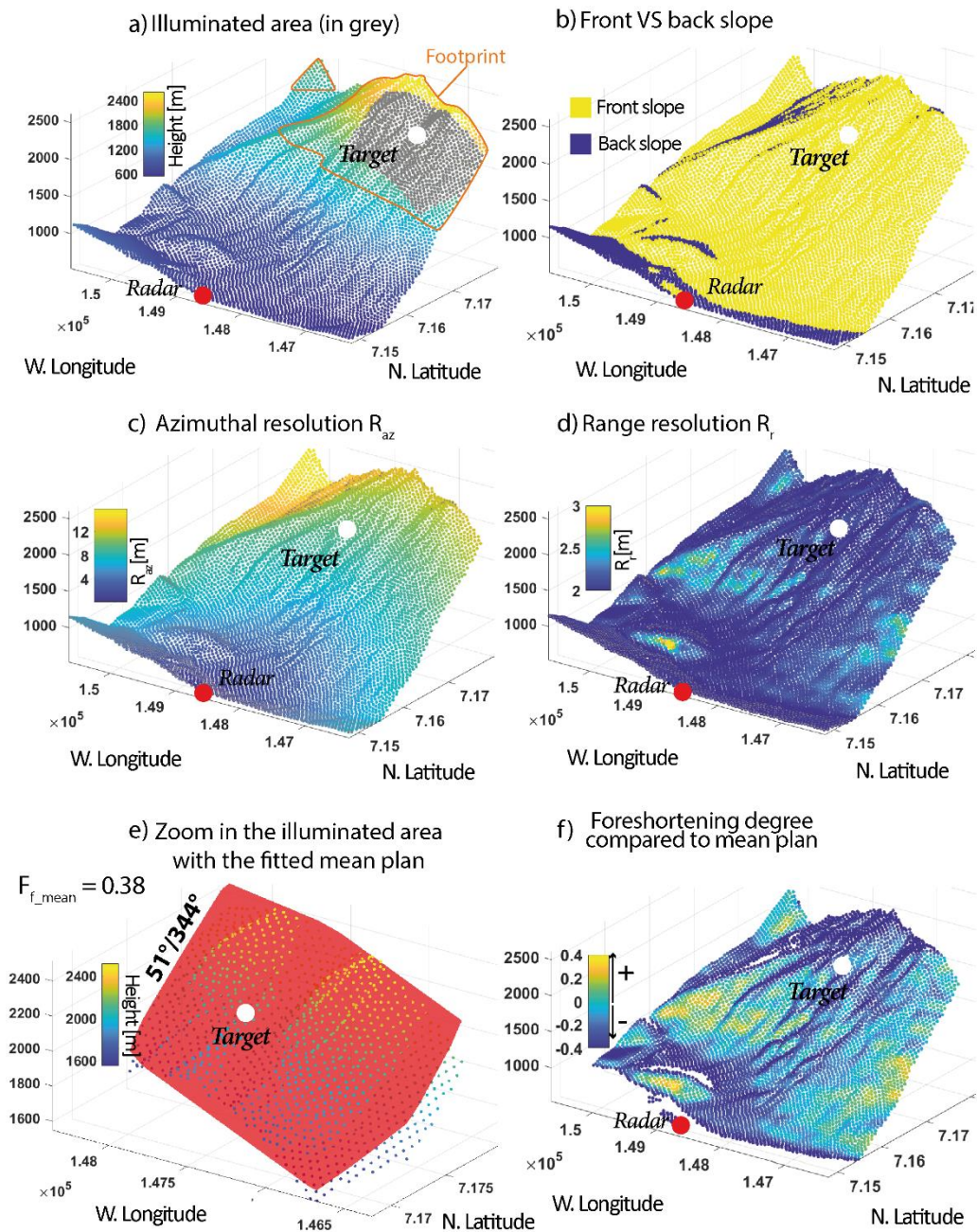
The LoS distance is almost at the limit of what is acceptable to have a backscattered signal (3351 m at the target location and 3900 m near the crest). Such a distance decreases considerably the azimuthal resolution, which varies between 8 m and 13 m along the range of the illuminated slope (Figure 15c) for a range resolution of 2.0 m (Figure 15d). The SoI is affected by a
385 constant and low foreshortening of 0.38 (Figure 15e, f).

5.1.3 La Cornalle (Figure 16, Figure A3)

The LoS distance is 267 m resulting in a good resolution in azimuth varying between 0.3 m and 0.7 m along the SoI (Figure 16c) and in range between 0.8 m and 1 m (Figure 16d). The slope is very steep, the apparent slope dip is 73°. Consequently, the radar image is affected by a strong foreshortening of 0.81 (Figure 16e). In the center of the slope illuminated by the radar
390 (Figure 16a), one can see a little terrace in backslope and affected by shadowing (Figure 16b). The slope below this terrace is less steep than the illuminated area mean plan oriented 61°/267° while the one located above is steeper. The lower part is less affected by foreshortening than the upper part (Figure 16f).



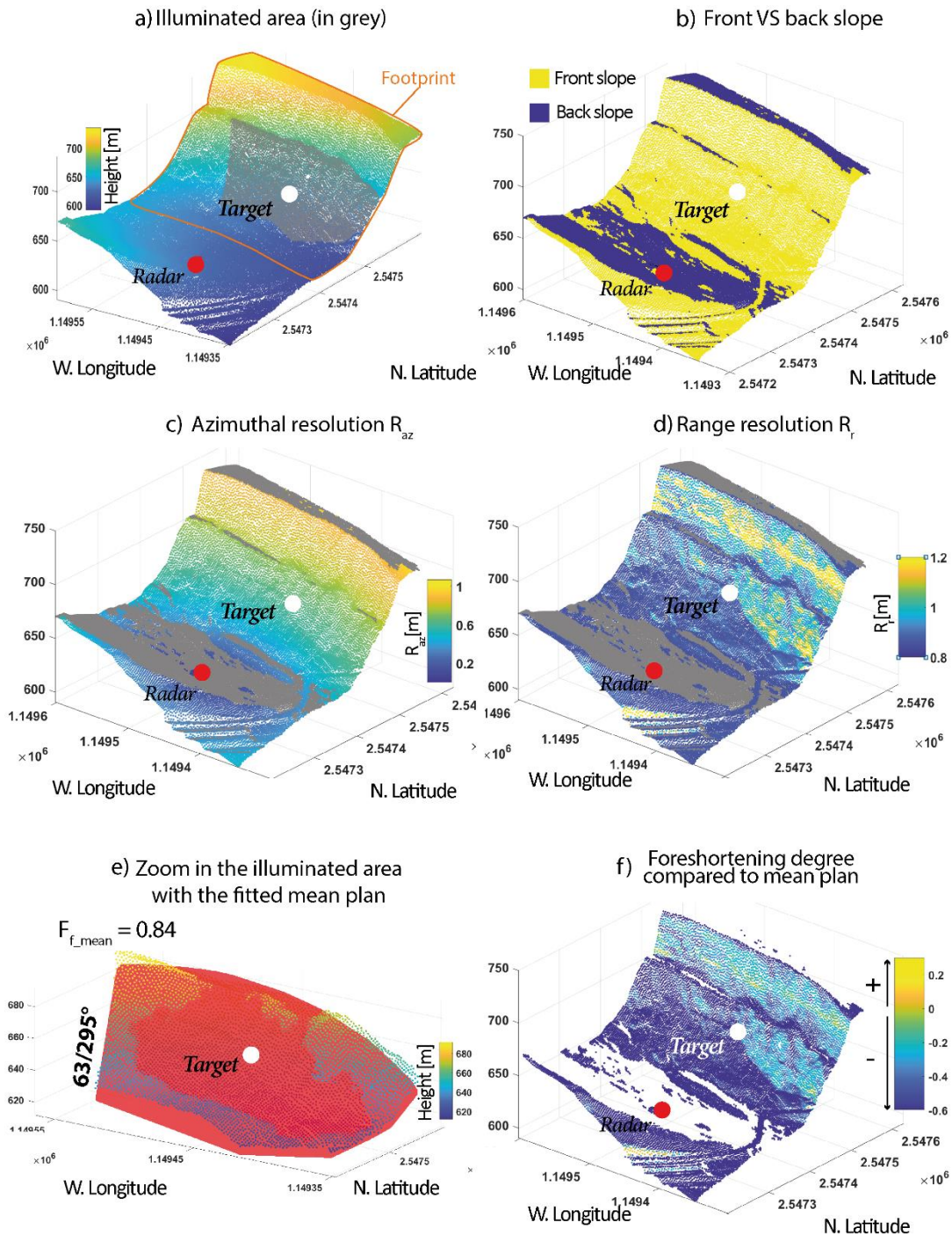
395 **Figure 14 : Output maps for the synthetic dataset. a) Illuminated area and footprint for the chosen parameters. b) Front VS back slope. The back slope corresponds to areas in shadow. c) The azimuthal resolution increases with the distance to the radar. d) The range resolution increases with the slope dip but in a same slope degree, it decreases from near- to far-range. e) Zoom in the illuminated area for which the mean plan is estimated. The mean dip of the area is 48° with a mean foreshortening of 0.67. f) Foreshortening degree compared to the mean plan one F_{f_MEAN} . Smoother slopes are less affected by the foreshortening than the mean plan. The steeper ones are more affected. The other output maps are presented in the Appendix A.**



400

405

Figure 15 : Output maps for the first dataset, Cima del Simano. a) Illuminated area and footprint for the chosen parameters. b) Front VS back slope. The back slope corresponds to areas in shadow. c), d) Azimuthal and range resolutions. Since the chosen bandwidth is 75 MHz to be sure to record the backscattered signal, the resolutions are poor. Only a monitoring of major volume instabilities is relevant here. e) Zoom in the illuminated area for which a mean plan fitting is estimated. The mean dip of the area is 51° with a mean foreshortening of 0.38. f) Foreshortening degree compared to the mean plan one. The lower part is more affected by foreshortening than the top of the mountain, which is the area of interest. The other output maps are presented in the Appendix B.



410 **Figure 16 : Output maps for the second dataset, La Cornalle cliff. a) Illuminated area and footprint for the chosen parameters. b) Front VS back slope. The back slope corresponds to areas in shadow. c), d) Azimuthal and range resolutions. Since the radar is only at a distance of 260 m, the selected bandwidth is 175 MHz to have a good range resolution. e) Zoom in the illuminated area for which a mean plan fitting is estimated. The mean dip of the area is 61° with a mean foreshortening of 0.81. f) Foreshortening degree compared to the mean plan one. The other output maps are presented in the Appendix C.**

6 Discussion

415 6.1 Comparison for three different radar locations

Figure 7 presented the impact of the radar location on the resulting image. To verify those concepts, three radar locations, P1, P2 and P3, have been selected on the study site of Cima del Simano to monitor the same region of interest. Their output characteristics are summarized and compared in Table 6. Locations P1 and P2 are located in front of the cliff and along the direction parallel to the slope dip; P1 being further away from the target area than P2. P3 is located almost at the same distance
420 of the cliff than P2 (P3 is 113 m further away from the target than P2) but looks at the target area from aside.

The results are coherent with what is expected from Table 2. An acquisition from P2 gives a better range resolution (2.01 m) compared to P1 (2.14 m). Those two points being located in front of the cliff, their apparent slope dip corresponds to the real one (64°), while the apparent slope dip for P3 is lower (60°) reducing slightly the range resolution (2.00 m). One could conclude that the best location for the acquisition is P3. Nonetheless this position triggers here more areas in shadow (backslope) leading
425 to a loss of information. Furthermore, the gravitational movements are often expected to follow the slope dip direction (Pedrazzini et al., 2010; Dehls et al., 2010). Looking to the target area from aside as with P3, the LoS direction is not parallel to the slope, the registered displacement may be lesser than the real one (Colesanti and Wasowski, 2006; Dai et al., 2022).

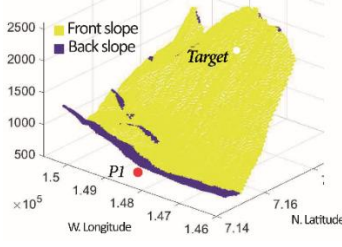
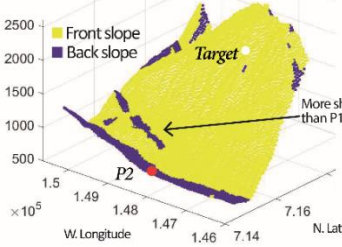
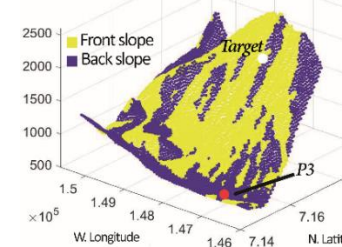
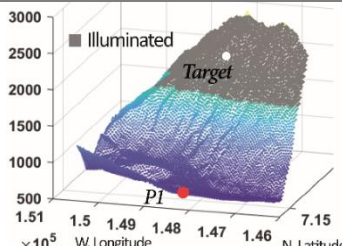
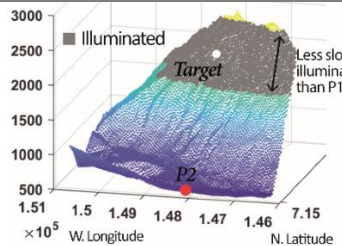
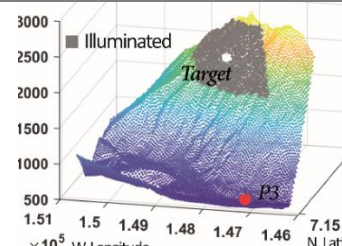
The illuminated area is wider in the case of P1 than with P2 or P3. If the unstable area to monitor is very large, P1 can be advantageous. Since the LoS distance remains smaller than 4 km (3.9 km); the backscattered signal is still registered from P1.
430 Thus, the best installation location highly depends on the purpose of the acquisition and the area of interest.

- If the main goal is to monitor a large area in order to detect unstable zones and estimate an average displacement rate such as in Carlà et al. (2019), a position far from the monitored cliff (similar to P1) should be considered. The tool can help checking that the LoS distance remains smaller than 4 or 5 km and estimating the extent of the illuminated area. But one must be aware that the resulting range and azimuthal resolutions of the radar image increase.
- If the main goal is to get the best resolution at the expense of the illuminated area size, one should try locating the
435 radar closer to the monitored cliff (similar to P2 and P3). It is the case for example when one tries to define the kinematic behavior (Frattini et al., 2018) or to assess the susceptibility to fail (Jaboyedoff et al., 2012) of massive rock instabilities. The tool helps checking which location (close to the cliff, in front of or aside the cliff) gives the best resolution while avoiding having the SoI in the shadow.

440

445

Table 6: Comparison of three different radar locations and the impact on their corresponding radar image. Advantages and drawbacks for each position are highlighted.

Corresponding position in Figure 7 Test case	P1 In front of the cliff Far from the cliff	P2 In front of the cliff Close to the cliff	P3 Aside the cliff
Coordinate system	CH1903 - LV03		
Target location	[717600 ; 147300 ; 2193]		
Radar location	[714108 ; 148128 ; 750]	[715400 ; 148700 ; 635]	[715201 ; 147193 ; 556]
Backslope			
Illuminated area			
dLoS	3927	3282	3150
app. Dip	64°	64°	60°
Azimuthal resolution	11.64	9.89	8.72
Range resolution	2.14	2.01	2.00
Advantages	- Wider extend of the illuminated surface	- Better resolutions than P1	- Better resolutions than P1 and P2
Drawbacks	- Compression of information in range - dLoS limit for recording backscattered signal	- Smaller illuminated surface than P1 - More shadow than P1	- More shadow than P1 and P2 - Measured displacement along the LoS may be lower than the real one

450 6.2 Tool limitations

Since the input of the program is a DEM converted into a 3D grid, the overhanging slopes, which are those subject to layover cannot be detected. To overcome this limitation, a suggestion could be to use a point cloud acquired from the ground with a LiDAR (Abellán et al., 2014) or by photogrammetry (Eltner and Sofia, 2020). But this comes with other problems, such as the potential occlusions (Sturzenegger et al., 2007) and noises due to the presence of vegetation and which can bias the
455 calculated dip and dip direction of the slope.

7 Conclusion and further development

This paper described the main features of a Linear GB-InSAR acquisition, emphasizing and comparing the significant differences from satellite radar acquisitions. While these distinctions are rarely addressed in the literature, they are crucial considerations for anyone initiating a GB-InSAR monitoring campaign.

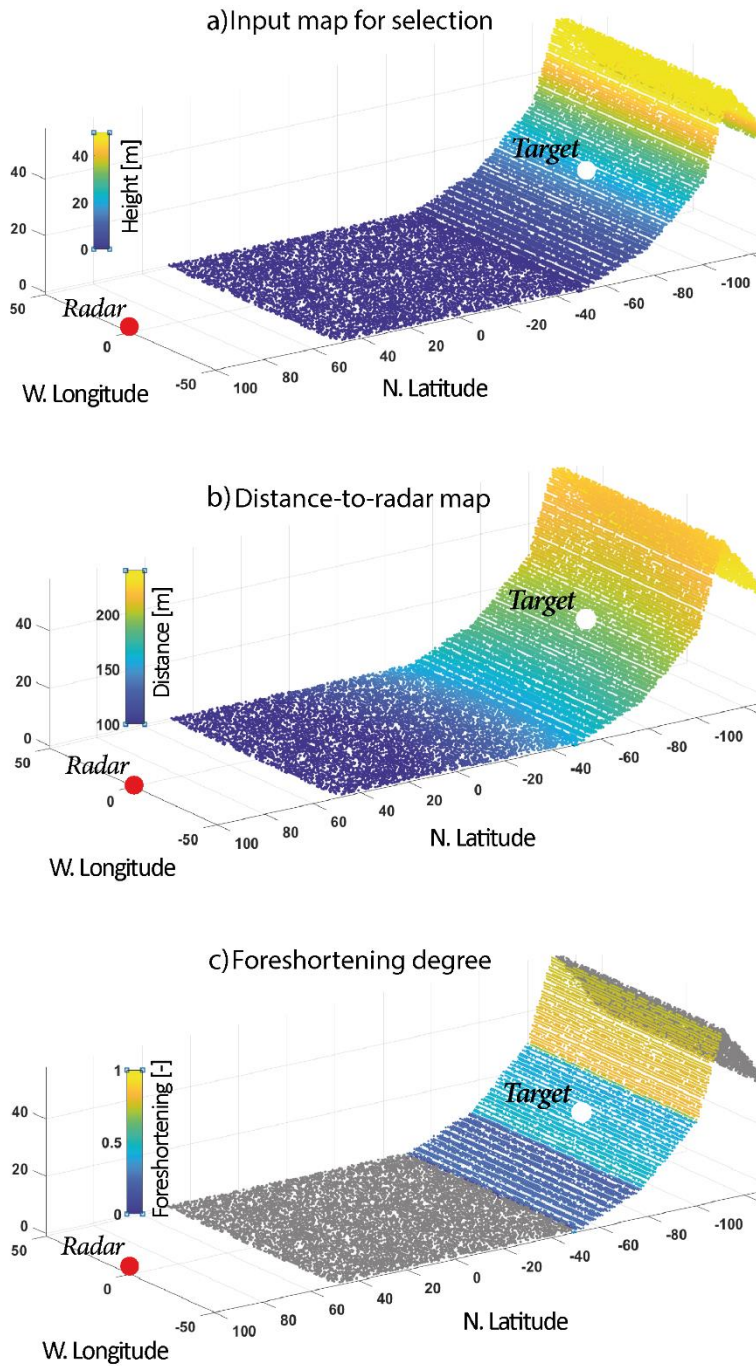
460 The paper introduces in a second step a novel MATLAB tool designed for the estimation of the characteristics of Linear GB-InSAR acquisitions. This tool generates a set of valuable maps, including the radar-to-target distance, range and azimuthal resolution, foreshortening degree, and shadowing maps in a single operation. The main purpose is to streamline the search for the optimal radar installation site, which guarantees the most effective monitoring results when multiple options are considered. Since the determination of the ideal location varies depending on the objectives of the acquisition campaign, providing
465 comprehensive information critical for selection simplifies the sensitive choice for the most suitable site.

If the purpose is to monitor a large area and to delimitate the unstable zone, the radar should be installed far from the cliff, using the MATLAB tool to check that the LoS distance remains below 4 or 5 km, depending on the GB-InSAR device. Contrariwise, if the purpose is to characterize the displacement gradient, one will try optimizing the resolution while keeping the LoS as parallel as possible to the displacement vector. In that case, the tool helps verifying and avoiding the foreshortening
470 and shadowing areas.

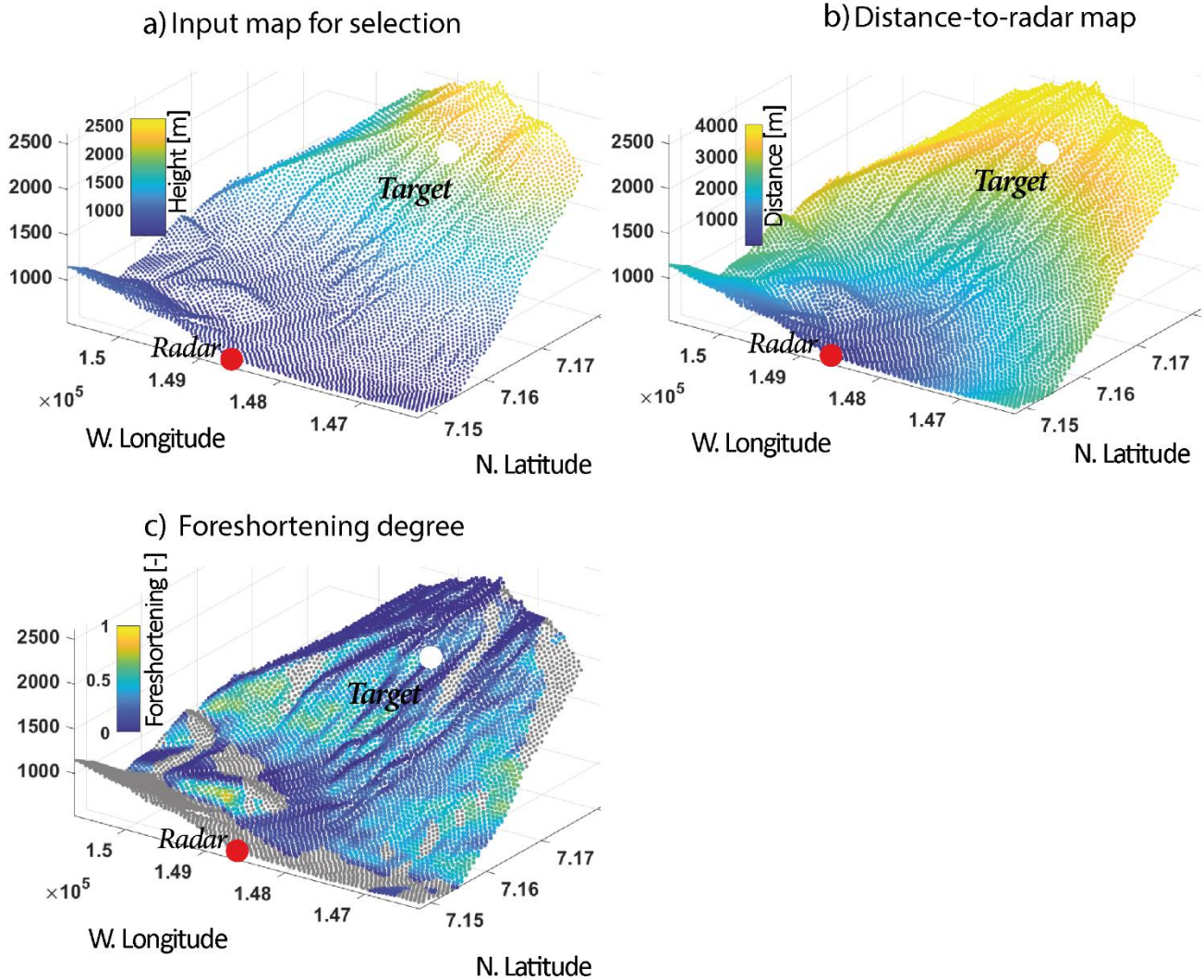
Nevertheless, the radar acquisition characteristics are often not the only thing to consider when choosing the best location. Most of the time, the electricity access and an easy installation on a flat surface, as well as the expected instability movement direction, reduce the choices (Caduff et al., 2015).

The tool could be improved and extended to the other GB-InSARs of type ArcSAR or rotary RAR (Pieraccini et Miccinesi
475 2019) and for the estimation of satellite InSAR images characteristics in order to select the best ascending or descending orbit acquisition before starting the downloading and treatment of the images which can also be a long and laborious work (Berardino et al. 2002; Mancini et al. 2021).

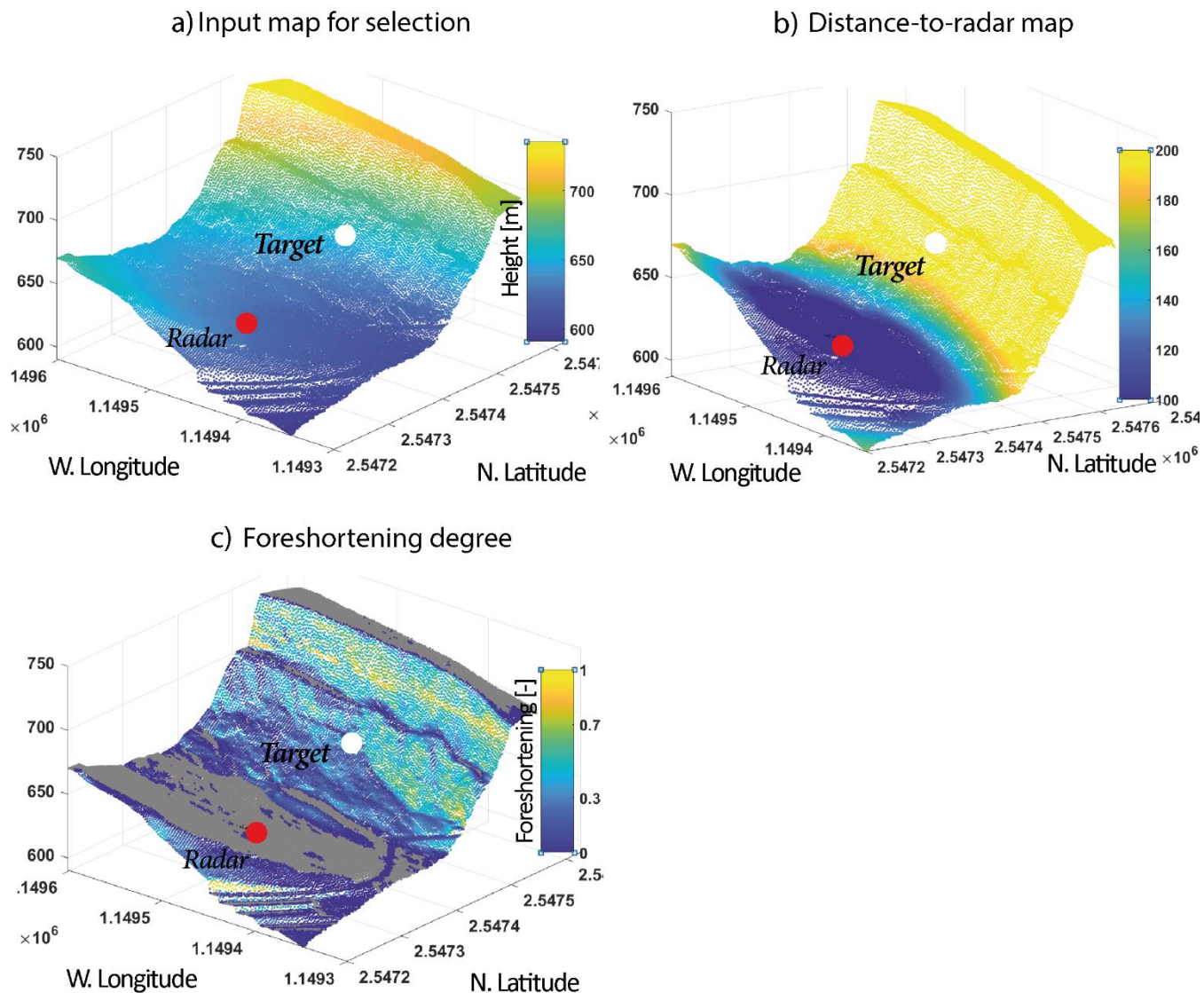
Appendix A



480 **Figure A1: Additional output map for the synthetic dataset. a) The input map with the altitude, aimed at choosing the radar and target location b) The distance-to radar map. The distance between the radar and the target should not be greater than 4 km. c) The foreshortening map, after the Equation 8.**



485 **Figure A2: Additional output map for the first dataset, Cima del Simano. a) The input map with the altitude, aimed at choosing the radar and target location b) The distance-to-radar map. The distance between the radar and the target should not be greater than 4 km. c) The foreshortening map, after the Equation 8.**



490 **Figure A3: Additional output map for the second dataset, La Cornalle. a) The input map with the altitude, aimed at choosing the radar and target location b) The distance-to-radar map. The distance between the radar and the target should not be greater than 4 km. c) The foreshortening map, after the Equation 8.**

Code and data availability

All raw data can be provided by the corresponding authors upon request. The code and the input point clouds are available on Github. (<https://github.com/charlottewolff/GB-PAR>)

495 **Author contributions**

MHD had the tool idea; CW wrote and tested the code; CW created the synthetic dataset and performed the acquisition of the real datasets; CR provided documentation for comparing satellite and GB- techniques; CW wrote the manuscript draft and edited the manuscript; MHD, CR, MJ reviewed the manuscript.

Competing interests

500 The contact author has declared that none of the authors has any competing interests.

References

- Abellán, A., Oppikofer, T., Jaboyedoff, M., Rosser, N. J., Lim, M., and Lato, M. J.: Terrestrial laser scanning of rock slope instabilities: STATE-OF-SCIENCE (TERRESTRIAL LiDAR VS. ROCK SLOPE INSTABILITIES), *Earth Surf. Process. Landforms*, 39, 80–97, <https://doi.org/10.1002/esp.3493>, 2014.
- 505 Addie, G.: A new true thickness formula based on the apparent dip, *Economic Geology*, 63, 188, <https://doi.org/10.2113/gsecongeo.63.2.188>, 1968.
- Anon: ETSI EN 300 440 v2.1.1, 2017.
- Antonello, G., Casagli, N., Farina, P., Fortuny, J., Leva, D., Nico, G., Sieber, A. J., and Tarchi, D.: A ground-based interferometer for the safety monitoring of landslides and structural deformations, in: IGARSS 2003. 2003 IEEE
510 International Geoscience and Remote Sensing Symposium. Proceedings (IEEE Cat. No.03CH37477), IGARSS 2003. 2003 IEEE International Geoscience and Remote Sensing Symposium., Toulouse, France, 218–220, <https://doi.org/10.1109/IGARSS.2003.1293729>, 2003.
- Berardino, P., Fornaro, G., Lanari, R., and Sansosti, E.: A new algorithm for surface deformation monitoring based on small baseline differential SAR interferograms, *IEEE Trans. Geosci. Remote Sensing*, 40, 2375–2383,
515 <https://doi.org/10.1109/TGRS.2002.803792>, 2002.
- Cabral-Cano, E., Dixon, T. H., Miralles-Wilhelm, F., Diaz-Molina, O., Sanchez-Zamora, O., and Carande, R. E.: Space geodetic imaging of rapid ground subsidence in Mexico City, *Geological Society of America Bulletin*, 120, 1556–1566, <https://doi.org/10.1130/B26001.1>, 2008.
- Caduff, R., Schlunegger, F., Kos, A., and Wiesmann, A.: A review of terrestrial radar interferometry for measuring
520 surface change in the geosciences: TERRESTRIAL RADAR INTERFEROMETRY IN THE GEOSCIENCES, *Earth Surf. Process. Landforms*, 40, 208–228, <https://doi.org/10.1002/esp.3656>, 2015.
- Carlà, T., Tofani, V., Lombardi, L., Raspini, F., Bianchini, S., Bertolo, D., Thuegaz, P., and Casagli, N.: Combination of GNSS, satellite InSAR, and GBInSAR remote sensing monitoring to improve the understanding of a large landslide in high alpine environment, *Geomorphology*, 335, 62–75,
525 <https://doi.org/10.1016/j.geomorph.2019.03.014>, 2019.

- Carrea, D., Abellán, A., Guerin, A., Jaboyedoff, M., and Voumard, J.: Erosion processes in molassic cliffs: the role of the rock surface temperature and atmospheric conditions, 2014.
- Carrea, D., Abellan, A., Derron, M.-H., and Jaboyedoff, M.: Automatic Rockfalls Volume Estimation Based on Terrestrial Laser Scanning Data, in: *Engineering Geology for Society and Territory - Volume 2*, edited by: Lollino, G., Giordan, D., Crosta, G. B., Corominas, J., Azzam, R., Wasowski, J., and Sciarra, N., Springer International Publishing, Cham, 425–428, https://doi.org/10.1007/978-3-319-09057-3_68, 2015.
- Casagli, N., Farina, P., Leva, D., Nico, G., and Tarchi, D.: Ground-based SAR interferometry as a tool for landslide monitoring during emergencies, in: *IGARSS 2003. 2003 IEEE International Geoscience and Remote Sensing Symposium. Proceedings (IEEE Cat. No.03CH37477)*, IGARSS 2003. 2003 IEEE International Geoscience and Remote Sensing Symposium., Toulouse, France, 2924–2926, <https://doi.org/10.1109/IGARSS.2003.1294633>, 2003.
- Catani, F., Canuti, P., and Casagli, N.: The Use of Radar Interferometry in Landslide Monitoring, in: *Landslides in Cold Regions in the Context of Climate Change*, edited by: Shan, W., Guo, Y., Wang, F., Marui, H., and Strom, A., Springer International Publishing, Cham, 177–190, https://doi.org/10.1007/978-3-319-00867-7_13, 2014.
- Cazzanil, L., Colesanti, C., Leva, D., Nesti, G., Prati, C., Roccal, F., Tarchi, D., and di Milano, P.: A ground based parasitic SAR experiment, *Geoscience and Remote Sensing, IEEE Transactions*, 38, 2132–2141, 2000.
- Colesanti, C. and Wasowski, J.: Investigating landslides with space-borne Synthetic Aperture Radar (SAR) interferometry, *Engineering Geology*, 88, 173–199, <https://doi.org/10.1016/j.enggeo.2006.09.013>, 2006.
- Dai, K., Deng, J., Xu, Q., Li, Z., Shi, X., Hancock, C., Wen, N., Zhang, L., and Zhuo, G.: Interpretation and sensitivity analysis of the InSAR line of sight displacements in landslide measurements, *GIScience & Remote Sensing*, 59, 1226–1242, <https://doi.org/10.1080/15481603.2022.2100054>, 2022.
- Dehls, J., Giudici, D., Farina, P., Martin, D., and Froese, D.: Monitoring Turtle Mountain using ground-based synthetic aperture radar (GB-InSAR). *GeoCalgary, GeoCalgary 2010*, Calgary, AB, Canada, 1635–1640, 2010.
- Eltner, A. and Sofia, G.: Structure from motion photogrammetric technique, in: *Developments in Earth Surface Processes*, vol. 23, Elsevier, 1–24, <https://doi.org/10.1016/B978-0-444-64177-9.00001-1>, 2020.
- Fei, L., Choanji, T., Derron, M.-H., Jaboyedoff, M., Sun, C., and Wolff, C.: Retreat analysis of a sandstone marl interbedded cliff based on a three-year remote sensing survey: A case study at La Cornalle, Switzerland, 2023.
- Ferretti, A., Monti-Guarnieri, A., Prati, C., Rocca, F., and Massonnet, D.: SAR images of the Earth’s surface, in: *InSAR Principles: Guidelines for SAR Interferometry Processing and Interpretation*, The Netherlands, 11–38, 2007.
- Ferretti, A., Rucci, A., Tamburini, A., Del Conte, S., and Cespa, S.: Advanced InSAR for Reservoir Geomechanical Analysis, in: *EAGE Workshop on Geomechanics in the Oil and Gas Industry, EAGE Workshop on Geomechanics in the Oil and Gas Industry*, Dubai, United Arab Emirates, <https://doi.org/10.3997/2214-4609.20140459>, 2014.

- 560 Frattini, P., Crosta, G. B., Rossini, M., and Allievi, J.: Activity and kinematic behaviour of deep-seated landslides from PS-InSAR displacement rate measurements, *Landslides*, 15, 1053–1070, <https://doi.org/10.1007/s10346-017-0940-6>, 2018.
- Gabriel, A. K., Goldstein, R. M., and Zebker, H. A.: Mapping small elevation changes over large areas: Differential radar interferometry, *J. Geophys. Res.*, 94, 9183, <https://doi.org/10.1029/JB094iB07p09183>, 1989.
- 565 Garthwaite, M. C., Miller, V. L., Saunders, S., Parks, M. M., Hu, G., and Parker, A. L.: A Simplified Approach to Operational InSAR Monitoring of Volcano Deformation in Low- and Middle-Income Countries: Case Study of Rabaul Caldera, Papua New Guinea, *Front. Earth Sci.*, 6, 240, <https://doi.org/10.3389/feart.2018.00240>, 2019.
- Goldstein, R. M., Zebker, H. A., and Werner, C. L.: Satellite radar interferometry: Two-dimensional phase unwrapping, *Radio Sci.*, 23, 713–720, <https://doi.org/10.1029/RS023i004p00713>, 1988.
- 570 Griffiths, H.: Interferometric synthetic aperture radar, *Electronics & Communications Engineering Journal*, 7, 247–256, <https://doi.org/10.1049/ecej:19950605>, 1995.
- Hein, A.: *Processing of SAR Data: Fundamentals, Signal Processing, Interferometry*, Springer, 2004.
- Henderson, F. M. and Lewis, A. J.: Radar Fundamentals: The Geoscience Perspective., in: *Principles and Application of Imaging Radar: Manual of Remote Sensing*, John Wiley, New York, 131–181, 1998.
- 575 Hilley, G. E., Bürgmann, R., Ferretti, A., Novali, F., and Rocca, F.: Dynamics of Slow-Moving Landslides from Permanent Scatterer Analysis, *Science*, 304, 1952–1955, <https://doi.org/10.1126/science.1098821>, 2004.
- Jaboyedoff, M., Blikra, L., Crosta, G. B., Froese, C., Hermanns, R., Oppikofer, T., Böhme, M., and Stead, D.: Fast assessment of susceptibility of massive rock instabilities, in: *Landslides and Engineered Slopes. Protecting Society through Improved Understanding*, 11th International and 2nd North American Symposium on Landslides, Banff, Canada, 459–465, 2012.
- 580 Jensen, J. R.: chap.9. Active and Passive Microwave Remote Sensing, in: *Remote Sensing of the Environment: An Earth Resource Perspective*, 2nd edition, 2006.
- Klauder, J. R., Price, A. C., Darlington, S., and Albersheim, W. J.: The Theory and Design of Chirp Radars, *Bell System Technical Journal*, 39, 745–808, <https://doi.org/10.1002/j.1538-7305.1960.tb03942.x>, 1960.
- 585 Kropatsch, W. G. and Strobl, D.: The generation of SAR layover and shadow maps from digital elevation models, *IEEE Trans. Geosci. Remote Sensing*, 28, 98–107, <https://doi.org/10.1109/36.45752>, 1990.
- Leva, D., Nico, G., Tarchi, D., Fortuny-Guasch, J., and Sieber, A. J.: Temporal analysis of a landslide by means of a ground-based SAR interferometer, *IEEE Trans. Geosci. Remote Sensing*, 41, 745–752, <https://doi.org/10.1109/TGRS.2003.808902>, 2003.
- 590 Lingua, A., Piatti, D., and Rinaudo, F.: REMOTE MONITORING OF A LANDSLIDE USING AN INTEGRATION OF GB-INSAR AND LIDAR TECHNIQUES, 2008.

- Lipson, S. G., Lipson, H., and Tannhauser, D. S.: Waves, in: Optical Physics, The press syndicate of the university of Cambridge, Cambridge, 15–35, 1995.
- 595 Mahafza, B. R.: Radar systems analysis and design using Matlab, Chapman & Hall/CRC, Boca Raton, 529 pp., 2000.
- Mancini, F., Grassi, F., and Cenni, N.: A Workflow Based on SNAP–StaMPS Open-Source Tools and GNSS Data for PSI-Based Ground Deformation Using Dual-Orbit Sentinel-1 Data: Accuracy Assessment with Error Propagation Analysis, *Remote Sensing*, 13, 753, <https://doi.org/10.3390/rs13040753>, 2021.
- 600 Massonnet, D., Rossi, M., Carmona, C., Adragna, F., Peltzer, G., Feigl, K., and Rabaute, T.: The displacement field of the Landers earthquake mapped by radar interferometry, *Nature*, 364, 138–142, <https://doi.org/10.1038/364138a0>, 1993.
- gradientm:
- McCandless, S. and Jackson, C.: Chapter 1. Principles of Synthetic Aperture Radar, in: Synthetic Aperture Radar Marine User’s Manual, NOAA, 2004.
- 605 Miron, D.: CHAPTER 2 - Antenna Fundamentals I, in: Small Antenna Design, 9–41, 2006.
- Nadav, L.: Radar, in: Encyclopedia of Physical Science and Technology (Third Edition), Academic Press, 497–510, 2003.
- Noferini, L., Pieraccini, M., Mecatti, D., Luzi, G., Atzeni, C., Tamburini, A., and Broccolato, M.: Permanent scatterers analysis for atmospheric correction in ground-based SAR interferometry, *IEEE Trans. Geosci. Remote Sensing*, 43, 1459–1471, <https://doi.org/10.1109/TGRS.2005.848707>, 2005.
- 610 Pedrazzini, A., Jaboyedoff, M., Derron, M.-H., Abellán, A., and Orozco, C. V.: Reinterpretation of displacements and failure mechanisms of the upper portion of Randa rock slide, *GeoCalgary 2010*, Calgary, AB, Canada, 2010.
- Pieraccini, M. and Miccinesi, L.: Ground-Based Radar Interferometry: A Bibliographic Review, *Remote Sensing*, 11, 1029, <https://doi.org/10.3390/rs11091029>, 2019.
- 615 Pipia, L., Fabregas, X., Aguasca, A., and Lopez-Martinez, C.: Atmospheric Artifact Compensation in Ground-Based DInSAR Applications, *IEEE Geosci. Remote Sensing Lett.*, 5, 88–92, <https://doi.org/10.1109/LGRS.2007.908364>, 2008.
- Rees, W. G.: Technical note: Simple masks for shadowing and highlighting in SAR images, *International Journal of Remote Sensing*, 21, 2145–2152, <https://doi.org/10.1080/01431160050029477>, 2000.
- 620 Rouyet, L., Kristensen, L., Derron, M.-H., Michoud, C., Blikra, L. H., Jaboyedoff, M., and Lauknes, T. R.: Evidence of rock slope breathing using ground-based InSAR, *Geomorphology*, 289, 152–169, <https://doi.org/10.1016/j.geomorph.2016.07.005>, 2017.

- Rudolf, H., Leva, D., Tarchi, D., and Sieber, A. J.: A mobile and versatile SAR system, in: IEEE 1999 International Geoscience and Remote Sensing Symposium. IGARSS'99 (Cat. No.99CH36293), IEEE 1999 International Geoscience and Remote Sensing Symposium. IGARSS'99, Hamburg, Germany, 592–594, <https://doi.org/10.1109/IGARSS.1999.773575>, 1999.
- Sabins, F. F.: Remote Sensing : Principles and Interpretation, 3rd Edition., 494 pp., 1997.
- Stimson, G. W.: chap.30. Meeting High Resolution Ground Mapping Requirements, in: Introduction to Airborne Radar, vol. PM56, SPIE PRESS, 393–424, 1998.
- 630 Strozzi, T., Antonova, S., Günther, F., Mätzler, E., Vieira, G., Wegmüller, U., Westermann, S., and Bartsch, A.: Sentinel-1 SAR Interferometry for Surface Deformation Monitoring in Low-Land Permafrost Areas, Remote Sensing, 10, 1360, <https://doi.org/10.3390/rs10091360>, 2018.
- Sturzenegger, M., Yan, M., Stead, D., and Elmo, D.: Application and limitations of ground-based laser scanning in rock slope characterization, in: Rock Mechanics: Meeting Society's Challenges and Demands, edited by: Eberhardt, E., Stead, D., and Morrison, T., Taylor & Francis, 29–36, <https://doi.org/10.1201/NOE0415444019-c4>, 2007.
- 635 Talich, M.: The Deformation Monitoring of Dams by the Ground-Based InSAR Technique - Case Study of Concrete Hydropower Dam Orlík, IJAEE, 3, <https://doi.org/10.15242/IJAEE.A0416051>, 2016.
- Tapete, D., Casagli, N., Luzi, G., Fanti, R., Gigli, G., and Leva, D.: Integrating radar and laser-based remote sensing techniques for monitoring structural deformation of archaeological monuments, Journal of Archaeological Science, 40, 176–189, <https://doi.org/10.1016/j.jas.2012.07.024>, 2013.
- 640 Tarchi, D.: Monitoring landslide displacements by using ground-based synthetic aperture radar interferometry: Application to the Ruinon landslide in the Italian Alps, J. Geophys. Res., 108, 2387, <https://doi.org/10.1029/2002JB002204>, 2003.
- 645 Tarchi, D., Ohlmer, E., and Sieber, A.: Monitoring of Structural Changes by Radar Interferometry, Research in Nondestructive Evaluation, 9, 213–225, <https://doi.org/10.1080/09349849709414475>, 1997.
- Toomay, J. C. and Hannen, P. J.: Radar Principles for the Non-specialist, 3rd edition., Scitech Publishing, 2004.
- Turner, I. L., Harley, M. D., Almar, R., and Bergsma, E. W. J.: Satellite optical imagery in Coastal Engineering, Coastal Engineering, 167, 103919, <https://doi.org/10.1016/j.coastaleng.2021.103919>, 2021.
- 650 Usai, S. and Hanssen, R.: Long time scale INSAR by means of high coherence features, Proc. Ers. Symposium, 414, 1997.
- Werner, C., Strozzi, T., Wiesmann, A., and Wegmüller, U.: A real aperture radar for ground-based differential interferometry, Proc. IGARSS, Boston, MA, 1–2, 2008.
- 655 Wicks, C., Thatcher, W., and Dzurisín, D.: Migration of Fluids Beneath Yellowstone Caldera Inferred from Satellite Radar Interferometry, Science, 282, 458–462, <https://doi.org/10.1126/science.282.5388.458>, 1998.

Wolberg, J.: Chapter 2: The method of Least Squares, in: *Data Analysis Using the Method of Least Squares: Extracting the Most Information from Experiments*, Germany, 31–49, 2006.

Frequency-Modulated Continuous-Wave Radar (FMCW Radar): www.radartutorial.eu.

660 Wolff, C., Jaboyedoff, M., Fei, L., Pedrazzini, A., Derron, M.-H., Rivolta, C., and Merrien-Soukatchoff, V.: Assessing the Hazard of Deep-Seated Rock Slope Instability through the Description of Potential Failure Scenarios, Cross-Validated Using Several Remote Sensing and Monitoring Techniques, *Remote Sensing*, 15, <https://doi.org/10.3390/rs15225396>, 2023.

Woodhouse, I. H.: chap.10. Imaging Radar, in: *Introduction to Microwave Remote Sensing*, CRC Press, 45, 2006.

665 Yung-Chieh Lin and Chiou-Shann Fuh: Distortion correction for digital cameras, in: *Proceedings SIBGRAPI'98. International Symposium on Computer Graphics, Image Processing, and Vision (Cat. No.98EX237)*, SIBGRAPI'98. International Symposium on Computer Graphics, Image Processing, and Vision, Rio de Janeiro, Brazil, 396–401, <https://doi.org/10.1109/SIBGRA.1998.722778>, 1998.

Zebker, H. A. and Villasenor, J.: Decorrelation in interferometric radar echoes, *IEEE Trans. Geosci. Remote Sensing*, 30, 950–959, <https://doi.org/10.1109/36.175330>, 1992.

670